AGU PUBLICATIONS

JGR

Journal of Geophysical Research: Solid Earth

RESEARCH ARTICLE
10.1002/2016JB013683

Key Points:
- We present new forms of FORC data that include remanent, induced, and transient FORCs
- These new FORC-like diagrams reveal more detail about magnetic domain states that cannot be recovered by conventional FORCs
- Such data can aid in the interpretation of rock magnetic data that are widely applied to tackling a range of Earth science questions

Supporting Information:
- Supporting Information S1

Correspondence to:
X. Zhao,
xiang.zhao@anu.edu.au

Citation:
Zhao, X., A. P. Roberts, D. Heslop, G. A. Paterson, Y. Li, and J. Li (2017), Magnetic domain state diagnosis using hysteresis reversal curves, *J. Geophys. Res. Solid Earth*, *122*, doi:10.1002/2016JB013683.

Received 25 OCT 2016
Accepted 7 JUN 2017
Accepted article online 8 JUN 2017

Magnetic domain state diagnosis using hysteresis reversal curves

Xiang Zhao[1], Andrew P. Roberts[1], David Heslop[1], Greig A. Paterson[2], Yiliang Li[3], and Jinhua Li[2]

[1]Research School of Earth Sciences, Australian National University, Canberra, ACT, Australia, [2]Key Laboratory of Earth and Planetary Physics, Institute of Geology and Geophysics, Chinese Academy of Sciences, Beijing, China, [3]Department of Earth Sciences, The University of Hong Kong, Hong Kong

Abstract We present results for a series of hysteresis measurements that provide information about remanent, induced, transient-free, and transient magnetization components. These measurements, and differences between measurement types, enable production of six types of first-order reversal curve (FORC)-like diagrams which only double the number of measurements involved in a conventional FORC measurement. These diagrams can be used to distinguish magnetic signatures associated with each domain state. When analyzing samples with complex magnetic mineral mixtures, the contrasting domain state signatures are mixed together in a traditional FORC diagram, but these signatures can be identified individually when using the various FORC diagrams discussed here. The ability to make different FORC measurements and to identify separately each magnetic component by investigating different magnetization types can provide much-improved understanding of the information provided by FORC diagrams. In particular, the transient hysteresis FORC diagram provides a method to measure the nucleation field of magnetic vortices and domain walls. We provide a simple explanation for FORC results from natural multidomain samples that are not explained by conventional domain wall pinning models. We also provide software for processing the different types of FORC data.

1. Introduction

Most natural materials respond in some way to magnetic fields. Iron-bearing minerals have diverse magnetic properties, including ferrimagnetic, antiferromagnetic, and (super) paramagnetic behavior and are sensitive to a range of environmental processes, which makes magnetic measurements extremely useful for assessing natural magnetic signals in rock magnetism, environmental magnetism, and paleomagnetism [e.g., *Dunlop and Özdemir*, 1997; *Liu et al.*, 2012]. Ferrimagnetic minerals carry permanent magnetic signals and are the minerals of greatest interest in these research areas. Magnetic hysteresis measurements [*Ewing*, 1882] provide a powerful means with which to detect magnetic domain state variations in such materials. The *Preisach* [1935] model is used widely to describe the magnetic hysteresis behavior of ferrimagnetic minerals. In its most common form [*Néel*, 1954], this model involves an assumption of independently distributed magnetic switching and interaction fields, which appears to be unrealistic for describing the magnetization of natural samples [*Dunlop*, 1968; *Dunlop et al.*, 1990; *Hejda and Zelinka*, 1990]. In contrast, first-order reversal curve (FORC) measurements [*Mayergoyz*, 1986; *Pike et al.*, 1999; *Roberts et al.*, 2000] provide a practical approach to assessing switching and interaction field distributions without making any such assumptions and are a powerful tool for investigating domain state, magnetostatic interactions, and nucleation and annihilation of vortex states or domain walls [e.g., *Pike et al.*, 1999; *Pike and Fernandez*, 1999; *Roberts et al.*, 2000; *Stancu et al.*, 2001; *Cherchez et al.*, 2004; *Egli*, 2006; *Roberts et al.*, 2014]. FORC diagrams are used commonly to gain qualitative information about the presence of magnetic materials with varying domain states and the presence or absence of magnetostatic interactions. For example, the commonly observed central ridge signature in sedimentary samples is used widely as an indicator of the presence of noninteracting biogenic magnetic minerals [e.g., *Chen et al.*, 2007; *Egli et al.*, 2010; *Roberts et al.*, 2012; *Yamazaki and Ikehara*, 2012; *Heslop et al.*, 2014]. FORC diagrams are also being used increasingly in a more quantitative manner through calculation of theoretical FORC distributions for individual components and initial attempts at component-by-component unmixing [*Egli et al.*, 2010; *Harrison and Lascu*, 2014; *Heslop et al.*, 2014; *Lascu et al.*, 2015; *Channell et al.*, 2016].

Although FORCs have been used successfully in various fields, questions remain about the manifestations of some domain states in FORC diagrams. For example, *Pike and Fernandez* [1999] studied submicron Co dots

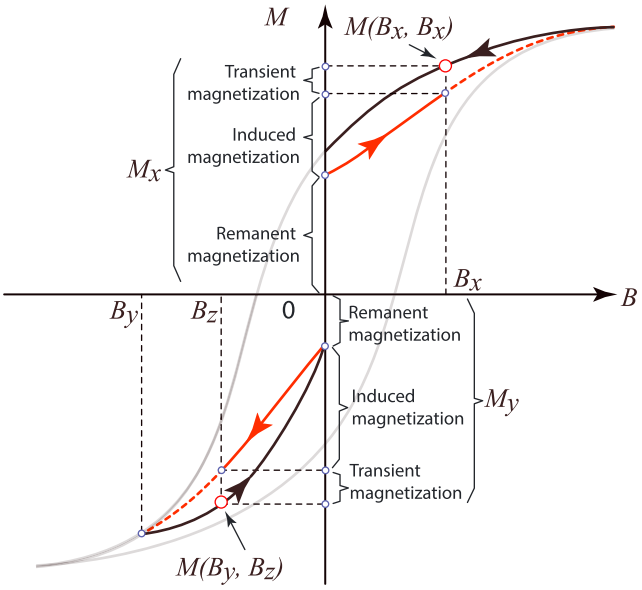

Figure 1. Definitions of the different types of magnetization discussed in this paper using a schematic hysteresis loop (gray line). The black lines with arrows indicate paths of changing magnetizations during hysteresis measurements (e.g., a major hysteresis loop or a FORC). The red lines with arrows indicate magnetization paths that start or pass through zero-field, which give the magnetization without a transient magnetization. Transient magnetization must be present in the magnetization path that decreases to zero field (black line) or in reversal curves for which the reversal field is not zero or of opposite sign.

and suggested that the magnetic vortex state should give rise to two positive regions and a possible extra butterfly pattern in FORC diagrams. However, these features have only been observed so far in synthetic samples with a narrow grain-size range [*Pike and Fernandez*, 1999; *Dumas et al.*, 2007a, 2007b; *Lappe et al.*, 2011, 2013] and in low-temperature FORC measurements [*Smirnov*, 2006, 2007; *Carvallo and Muxworthy*, 2006]. Hysteresis mechanisms in multidomain (MD) samples have also been analyzed using FORC diagrams [*Pike et al.*, 2001a], and it has been concluded that the classical domain wall pinning model of *Néel* [1955] does not explain the behavior of natural MD samples. FORC diagrams are also not optimal for detecting magnetic minerals with weak magnetizations, such as hematite, when they cooccur with strongly magnetized minerals, such as magnetite [*Muxworthy et al.*, 2005; *Carvallo et al.*, 2006a; *Paterson et al.*, 2010; *Roberts et al.*, 2014]. We explore these issues in the present paper and present additional FORC-type diagrams to enable these issues to be addressed in applications that require routine magnetic domain state diagnosis.

The total magnetization in a FORC measurement ($M_{FORC}(B_r, B)$) represents contributions from the remanent magnetization, induced magnetization, transient hysteretic magnetization [*Fabian and von Dobeneck*, 1997; *Fabian*, 2003; *Yu and Tauxe*, 2005], and thermal activation effects, which can be described as

$$M_{FORC}(B_r, B) = M_{rem}(B_r, B) + M_{induced}(B_r, B) + M_{TH}(B_r, B) + M_{thermal}(B_r, B), \quad (1)$$

where M_{FORC} represents the magnetization measured at a (B_r, B) location (where B_r is the reversal field at which a FORC measurement begins and B is the field at which individual magnetization measurements are made), M_{rem} is the remanent magnetization that remains when the applied field is removed, $M_{induced}$ is the induced magnetization that represents the magnetization added to M_{rem} when the field changes from zero to a nonzero field, M_{TH} is the transient hysteresis contribution that represents the magnetization difference between upper and lower magnetization curves when the lower curve starts from zero field (Figures 1 and 2c), and $M_{thermal}$ is the thermal activation effect. Thermal activation effects [e.g., *Pike et al.*, 2001b] will have different manifestations in the different types of FORC diagrams discussed in this paper, and as represented in each term of equation (1). Thus, we simplify equation (1) as follows:

$$M_{FORC}(B_r, B) = M_{rem}(B_r, B) + M_{induced}(B_r, B) + M_{TH}(B_r, B). \quad (2)$$

FORC diagrams provide a complex representation of these types of magnetization. In this paper, we present a range of approaches that allow FORC diagrams to be deconvolved to enable independent assessment of the contributions of different types of magnetization. These approaches will help to unlock a greater range of information and assist with interpretation of FORC diagrams for diagnosing the presence of different magnetic domain states in samples.

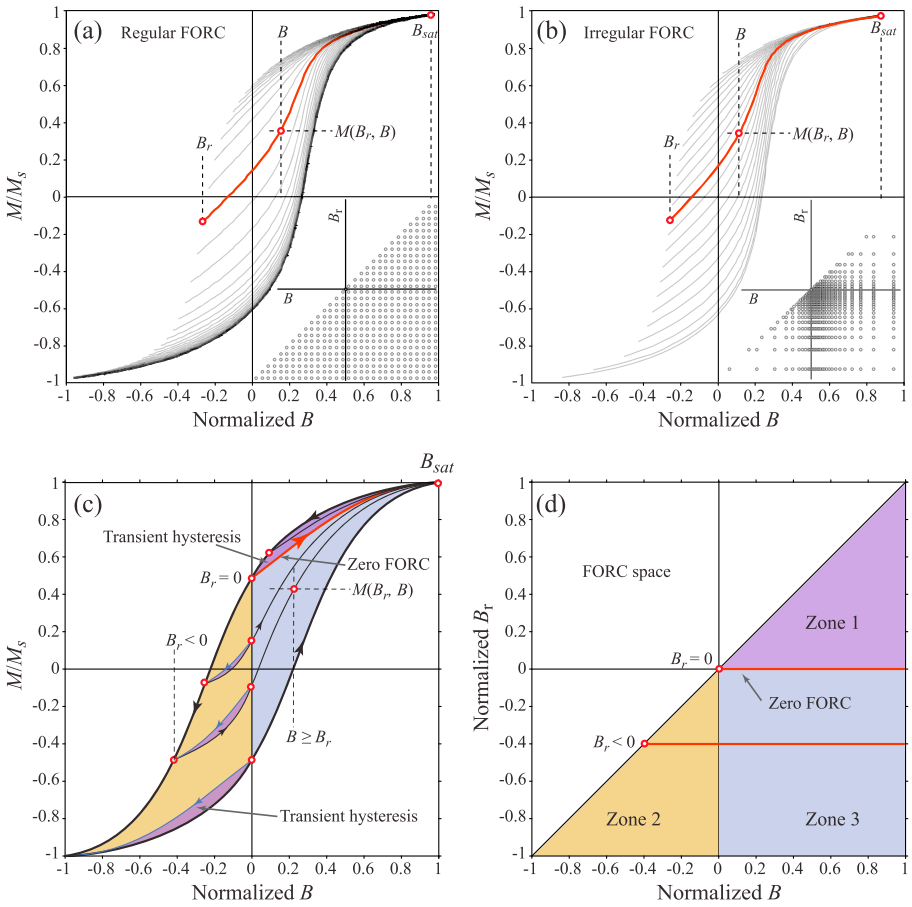

Figure 2. FORC definitions used throughout this paper. (a and b) Series of first-order reversal curves used to calculate a FORC distribution $\rho(B_r, B)$ from equation (1). Each reversal curve starts from a new reversal field B_r; the magnetization is measured at each field B up to the saturating field B_{sat}, where the magnetization at any measurement point is $M(B_r, B)$. Regular grid of measurement points for a series of FORCs (Figure 2a). The regular grid approach has been the standard since *Pike et al.* [1999]. Irregular grid of measurement points for a series of FORCs, which is defined by measuring a major hysteresis loop to determine a measurement grid where the greatest density of measurement points occurs where the magnetization changes the most (Figure 2b) [*Zhao et al.*, 2015]. The irregular grid protocol is used throughout this paper. (c) Major hysteresis loop with definition of important concepts such as transient hysteresis [*Fabian*, 2003] and the zero-FORC [*Yu and Tauxe*, 2005]. The color-coding indicates the regions of a set of FORC measurements that correspond to (d) different zones of a FORC diagram. In zone 1, transient and induced magnetizations make a contribution, transient and induced magnetizations contribute to zone 2 along with thermally activated contributions, and transient-free components (remanent and induced magnetizations) contribute to zone 3.

2. Methods

2.1. FORC Measurements

A FORC diagram is calculated from a class of partial hysteresis curves known as first-order reversal curves [*Mayergoyz*, 1986]. Each FORC is measured by saturating the sample with a large positive applied field. The field is then decreased to a reversal field B_r, and the FORC is the in-field magnetization curve that is measured at a series of applied fields B from B_r to the saturating field B_{sat} (Figure 2a). The magnetization at any field B with reversal field B_r is denoted as $M_{FORC}(B_r, B)$, where $B \geq B_r$. In a FORC measurement routine, multiple FORCs are measured for a range of B_r values to obtain the gridded set of magnetization measurements needed to create a FORC diagram. A FORC distribution is defined as the mixed second derivative:

$$\rho_{FORC}(B_r, B) \equiv -\frac{\partial^2 M_{FORC}(B_r, B)}{2\partial B_r \partial B}, \quad (3)$$

which is well defined only for $B \geq B_r$ [*Pike et al.*, 1999; *Roberts et al.*, 2000, 2014].

A FORC distribution $\rho_{FORC}(B_r, B)$ is calculated by fitting a second-order polynomial surface to a number of selected magnetization data points, the number of which depends on the smoothing factor (SF) and on the algorithm used to calculate the distribution (see *Roberts et al.* [2014] for details). SF is kept constant in the conventional FORC calculation process; this produces low resolution in peak regions for larger SF values, or a low signal-to-noise ratio in regions with little magnetization change when using small SF. The VariFORC [*Egli*, 2013] and irregular FORC [*Zhao et al.*, 2015] protocols provide optimized algorithms, where the former operates with traditional high-density measurements on a regular FORC grid (e.g., Figure 2a), while the irregular FORC measurement protocol makes use of information from a major hysteresis loop to define a grid with irregularly spaced measurements (e.g., Figure 2b). In the irregular grid protocol, measurements have highest density where the magnetization changes the most and *vice versa*. In this paper, all FORC data were measured and processed with the irregular FORC protocol of *Zhao et al.* [2015]. Generally, FORC diagrams are presented in terms of the interaction field B_i and coercivity B_c distributions using the transformations $B_i = (B_r + B)/2$ and $B_c = (B_r - B)/2$ and are rotated by 45° to enable presentation with these axes [*Pike et al.*, 1999]. In this paper, we present FORC diagrams in the original B_r and B coordinate system with B_i and B_c plotted along the diagonals.

2.2. Remanent FORC (remFORC) Measurements

Stancu et al. [2006] and *Bodale et al.* [2011] made FORC-like remanent magnetization measurements ($M_r(B_r, B)$) instead of in-field magnetization measurements ($M(B_r, B)$), which they refer to as a second-order reversal curve (SORC). *Church et al.* [2016] also studied remanent FORC distributions. Here we use a similar protocol to *Stancu et al.* [2006] but refer to SORCs as remFORC measurements. The remFORC distribution $\rho_{remFORC}(B_r, B)$ is defined as:

$$\rho_{remFORC}(B_r, B) \equiv -\frac{\partial^2 M_{rem}(B_r, B)}{2\partial B_r \partial B}. \quad (4)$$

Procedures for making FORC and remFORC measurements are illustrated in Figure 3. We made remFORC measurements with the same irregular measurement grid, data processing algorithm, and smoothing used in the irregular FORC protocol [*Zhao et al.*, 2015]. A benefit of this approach is that it enables comparison of both types of FORC diagram at the same resolution. The requirement to sweep the field to a specified value and back to $B = 0$ for remFORC measurements means that such measurements take about twice as long as equivalent FORC measurements (Figure 3). While this might be seen as a disadvantage by some users, we argue from the evidence provided below that the interpretive value of these additional measurements outweighs the disadvantage of the longer measurement time.

2.3. Transient Hysteresis FORC and Transient-Free Measurements

Fabian [2003] introduced the concept of transient hysteresis, which represents the minor hysteresis loop between the positive saturation field and zero-field (Figure 2c). The ascending branch of the hysteresis loop that starts from zero-field has been referred to as the zero-FORC [*Yu and Tauxe*, 2005]. Magnetization values from the descending branch have contributions from transient hysteretic magnetizations, while those from the ascending curve are free of transient hysteretic magnetization. The difference (or gap) between the descending and ascending branches of the loop is caused by internal self-demagnetization in coarse-grained magnetic particles. In the full FORC space (i.e., the colored triangular region in Figure 1d), FORCs with $B_r \geq 0$ only map the positive transient hysteresis (zone 1), while the $B < 0$ part of the FORC space with $B_r < 0$ (zone 2) provides a measure of the negative transient hysteresis (Figure 2d). Based on the definition of transient hysteresis, the transient hysteretic magnetization will decay to zero when the applied field returns to zero and will stay at zero even when the field increases. The transient hysteresis-free FORC (tfFORC) distribution can, thus, be determined by measuring the transient hysteresis-free magnetization (M_{tfFORC}) from the ascending curve that starts from zero at locations (B_r, B) by always ramping both B_r and B from zero field. In a transient-free hysteresis measurement, fields are always applied in the same direction, so that only field-driven magnetization reversal occurs. The tfFORC distribution $\rho_{tfFORC}(B_r, B)$ is defined as:

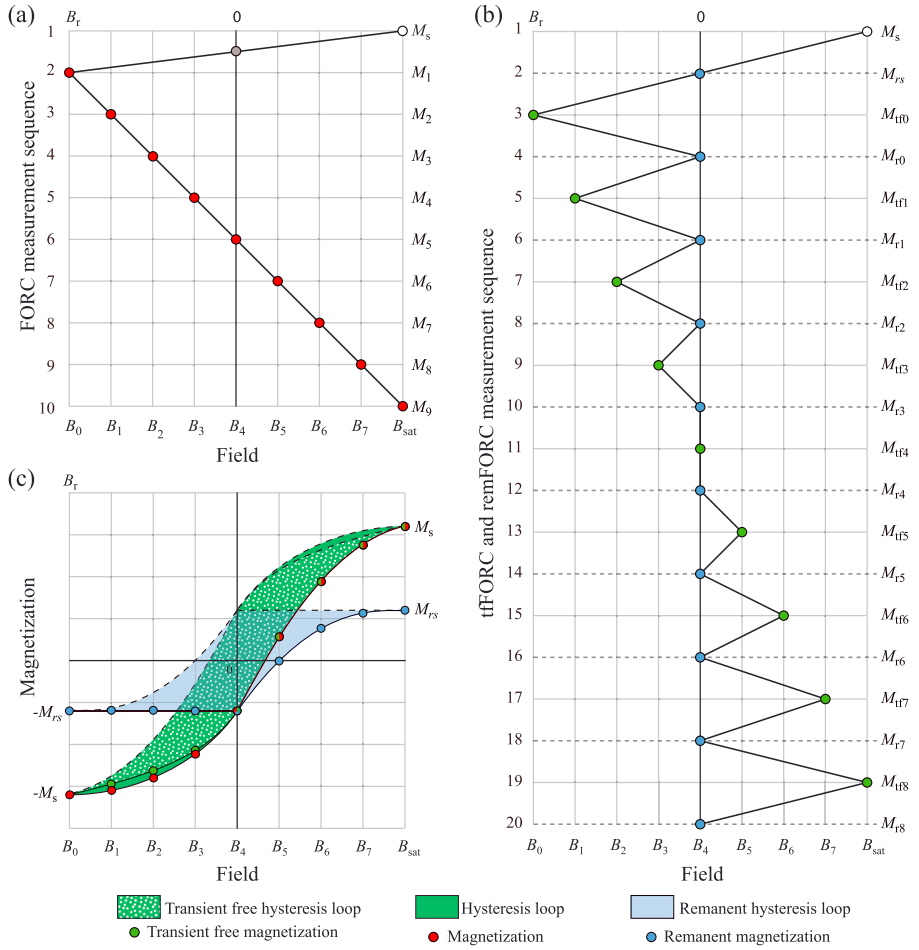

Figure 3. Comparison of measurement schemes for different types of FORC measurements discussed in this paper. (a) Schematic illustration of a sequence of conventional FORC measurements, starting from measurement of the saturation magnetization M_s, ramping the field to the initial reversal field B_0 and measuring the magnetization at regularly spaced fields B_1, … B_7 and back to B_{sat}. Such measurement sequences are repeated for each successive FORC, as indicated in the regular or irregular measurement grids in Figures 1a and 1b. (b) Schematic illustration of a sequence of transient-free FORC and remanence FORC (remFORC or SORC [*Stancu et al.*, 2006]) measurements, starting from measurement of M_s and ramping the field to zero to measure the saturation remanent magnetization M_{rs} and then ramping to the initial reversal field B_0. After application of each field B_0, … B_7 ($B_0 < B_1 < \ldots < B_7$), the field is switched off and the remanent magnetization M_{r0}, … M_{r8} is measured in zero-field. Such measurement sequences are repeated for each successive FORC, as indicated in the regular and irregular measurement grids in Figures 1a and 1b. (c) Color coded sequence of measurement points, which illustrates how the respectively colored measurements in Figures 3a and 3b contribute to in-field FORC and remanence FORC measurements, respectively. The dark green part of the FORC measurement represents the transient hysteresis contribution.

$$\rho_{\mathrm{tfFORC}}(B_r, B) \equiv -\frac{\partial^2 M_{\mathrm{tfFORC}}(B_r, B)}{2\partial B_r \partial B}. \tag{5}$$

The transient hysteresis FORC (tFORC) is then obtained by subtracting the tfFORC from FORC measurements for the same sample. Then M_{TH} can be calculated by $M_{\mathrm{TH}} = M_{\mathrm{FORC}} - M_{\mathrm{tfFORC}}$, and the tFORC distribution is defined as:

$$\rho_{\mathrm{tFORC}}(B_r, B) \equiv -\frac{\partial^2 M_{\mathrm{TH}}(B_r, B)}{2\partial B_r \partial B}. \tag{6}$$

Transient hysteresis-free FORC measurements, like remFORC measurements, take about twice as long to measure as equivalent FORC measurements. A typical set of FORC measurements (80 FORCs with 200 ms

averaging time) on an irregular grid takes about 2 h, while remFORC and tfFORC measurements are made during the same measurement sequence (Figure 3b), which takes about 4 h to complete. Thus, a sequence of all three measurement types takes ~6 h to complete. Such measurements could also be performed on a regular grid, but the sequence will take much longer to measure with little improvement in the FORC distributions. The regular grid method is defined using field steps, and the irregular grid method is defined using magnetization differences, so it is difficult to compare their relative efficiencies. From *Zhao et al.* [2015], 80 irregular FORCs are roughly equivalent to a minimum of 115 regular FORCs, but comparison will vary from sample to sample. As demonstrated below, six types of FORC distribution can be calculated from these three types of FORC measurements, and from differences between any two such measurements. These additional diagrams provide considerable diagnostic advantages that enable enhanced component-by-component interpretation of a conventional FORC diagram.

2.4. Differences Between FORCs

The difference between tfFORC and remFORC measurements provides the FORC distribution associated purely with the induced magnetization, while the difference between FORC and remFORC measurements represents a combination of tFORC and the induced magnetization. The induced FORC distribution $\rho_{\text{inducedFORC}}(B_r, B)$ is defined as:

$$\rho_{\text{inducedFORC}}(B_r, B) \equiv -\frac{\partial^2 M_{\text{induced}}(B_r, B)}{2\partial B_r \partial B} \equiv -\frac{\partial^2 (M_{\text{tfFORC}}(B_r, B) - M_{\text{rem}}(B_r, B))}{2\partial B_r \partial B}. \quad (7)$$

The difference between tfFORC and remFORC measurements can be determined in two ways. One is to calculate directly the difference among various types of processed FORC distributions. The other is to calculate magnetization differences from FORC measurements, and then to process the differential magnetization with the same algorithm and SF used for standard FORC processing. For the results presented here, we calculated magnetization differences from FORC measurements, but for the specimens measured here both procedures produce equivalent results.

3. Results

3.1. FORC Diagrams for Dominantly Stable SD Materials

A Verbatim 3.5″ floppy magnetic recording disk consists largely of thermally blocked stable SD magnetic particles [e.g., *Roberts et al.*, 2014]. For such stable SD particles, the FORC, tfFORC, and remFORC diagrams are similar (Figures 4a–4c). They all have a positive peak at $B_c \approx 100$ mT, with distributed coercivities and spreading parallel to the B_i axis. The only obvious difference is that a negative region occurs in the FORC and tfFORC diagrams, which is not present in the remFORC diagram. Instead, there is a weak positive peak at the same location in the remFORC diagram, which is almost invisible due to its low intensity compared with the main positive peak. The tFORC diagram (Figure 4d) has a larger positive peak along the $B_i < 0$ axis, and a smaller positive peak for $B_i > 0$, with a pair of small negative and positive peaks on both sides of the B_c axis that are not statistically significant. The induced magnetization component represented by the difference between the tfFORC and remFORC diagrams (Figure 4e) has three main peaks. One negative peak close to the $B_i < 0$ axis in zone 2 (see Figure 2d for a depiction of FORC zones) is associated with the stable SD state [*Muxworthy et al.*, 2004; *Newell*, 2005; *Muxworthy and Roberts*, 2007; *Roberts et al.*, 2014]. This peak is present in the induced magnetization FORC diagram (Figure 4e) but disappears in the remFORC diagram (Figure 4c), which indicates that it is contributed by the induced magnetization. A positive peak is located below the B_c axis in the induced FORC diagram, and another negative peak occurs above the B_c axis with a slightly higher B_c value. The difference between the FORC and remFORC diagrams (Figure 4f) contains all of the features in the tFORC and induced FORC diagrams. Results for a stable SD hematite sample from regolith in the south pit of Lancefield gold mine, Western Australia, are shown in Figure 5. The same characteristics of stable SD behavior are evident in both Figures 4 and 5, which indicates that this type of magnetic behavior is represented adequately by the procedures described here. Additionally, transient hysteresis effects are evident in tFORC diagrams (Figures 4d and 5d) for these two SD dominated samples. These effects are discussed further in section 4.2.

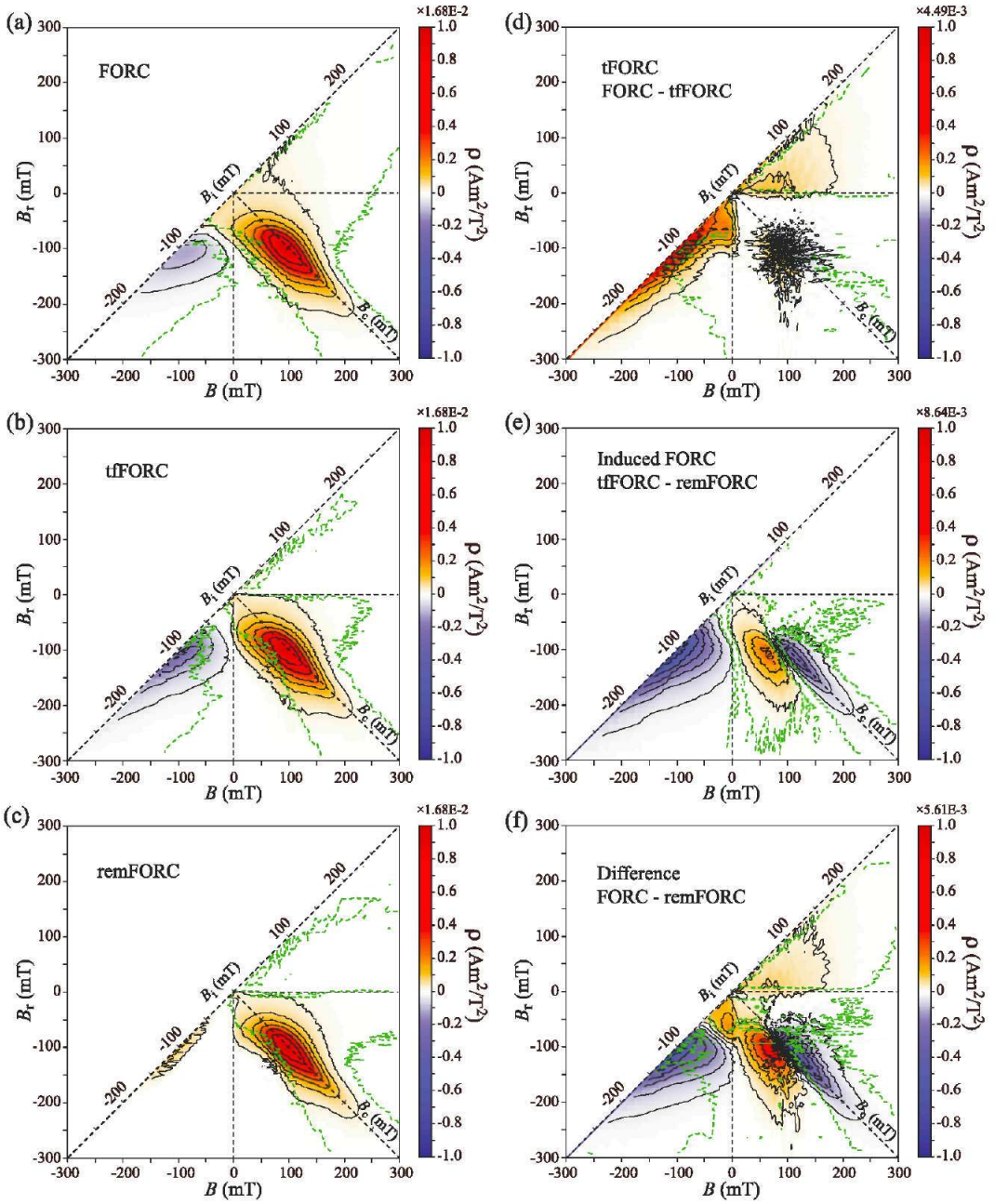

Figure 4. Sequence of six FORC diagrams that result from the three types of FORC measurements described here, and differences between the FORC measurements. The respective types of FORC diagrams are described in more detail in the main text. Results in this figure are for a floppy magnetic recording disk with stable SD magnetic properties [see *Roberts et al.*, 2014]. (a) Conventional FORC diagram, (b) transient-free (tf) FORC diagram, (c) remanent FORC diagram, (d) transient FORC diagram (=FORC-tfFORC), (e) induced FORC diagram (=tfFORC-remFORC), and (f) FORC-remFORC diagram. The green dashed lines represent 0.05 significance levels calculated following *Heslop and Roberts* [2012]. See text for discussion.

3.2. FORC Diagrams for Dominantly Vortex State Samples

An andesite sample from Mount Ruapehu, New Zealand, which is dominated by "pseudo-single domain" (PSD) magnetic behavior, was measured with the same irregular FORC grid [*Zhao et al.*, 2015] for FORC, tfFORC, and remFORC measurements. The FORC diagram has a coercivity peak at $B_c \sim 8$ mT, and spreading of the FORC distribution along the B_i axis (Figure 6a). The tfFORC and remFORC diagrams have a similar pattern in the $B > 0$ and $B_r < 0$ region (i.e., zone 3 of a FORC diagram), with different features outside this region along the B_i axis (Figures 6b and 6c). The tfFORC diagram has positive and negative features located in the $B_i > 0$ and $B_i < 0$

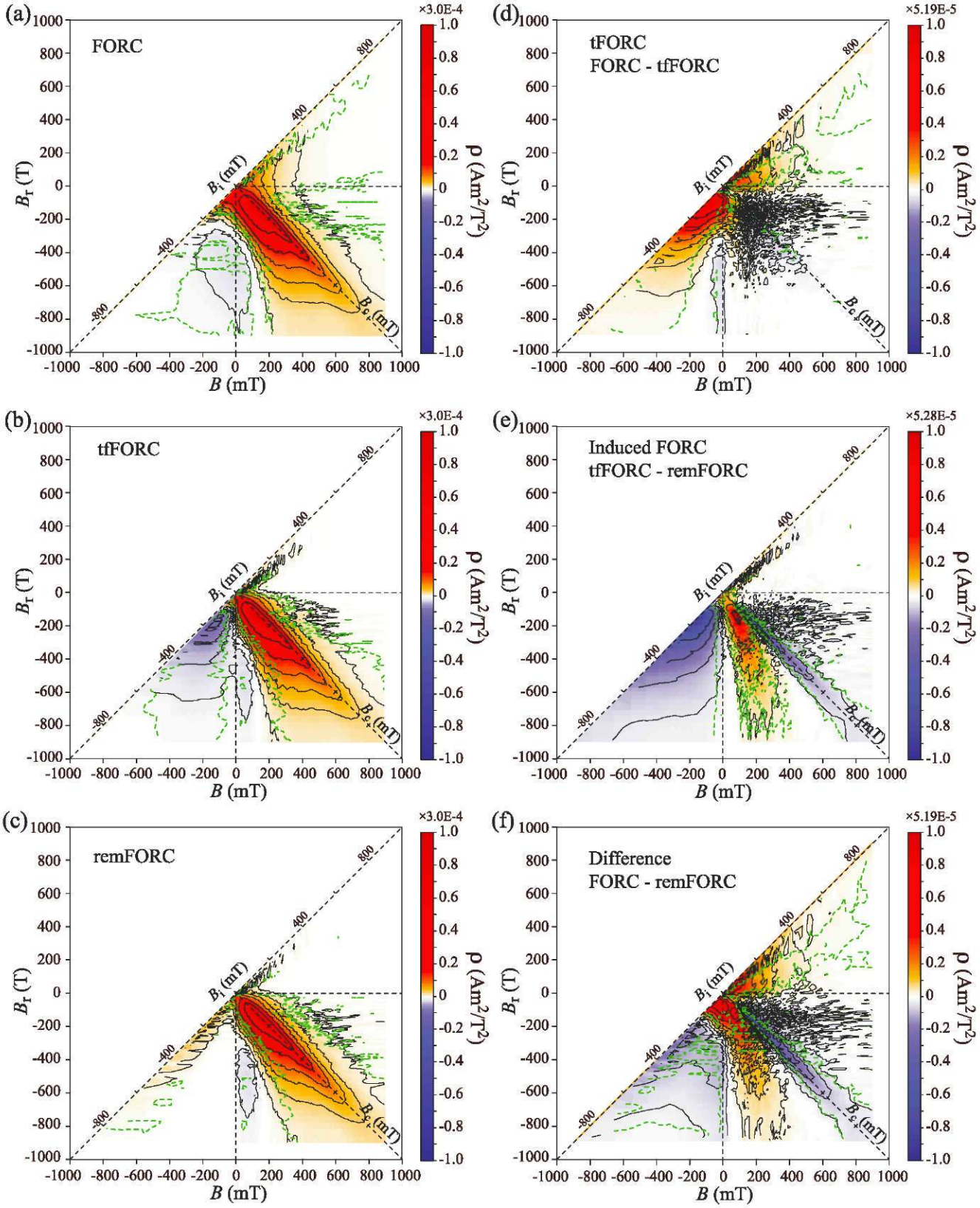

Figure 5. Sequence of six FORC diagrams for a stable SD hematite sample. (a) Conventional FORC diagram, (b) tfFORC diagram, (c) remFORC diagram, (d) tFORC diagram, (e) induced FORC diagram, and (f) FORC-remFORC diagram. The green dashed lines represent 0.05 significance levels calculated following *Heslop and Roberts* [2012]. See text for discussion.

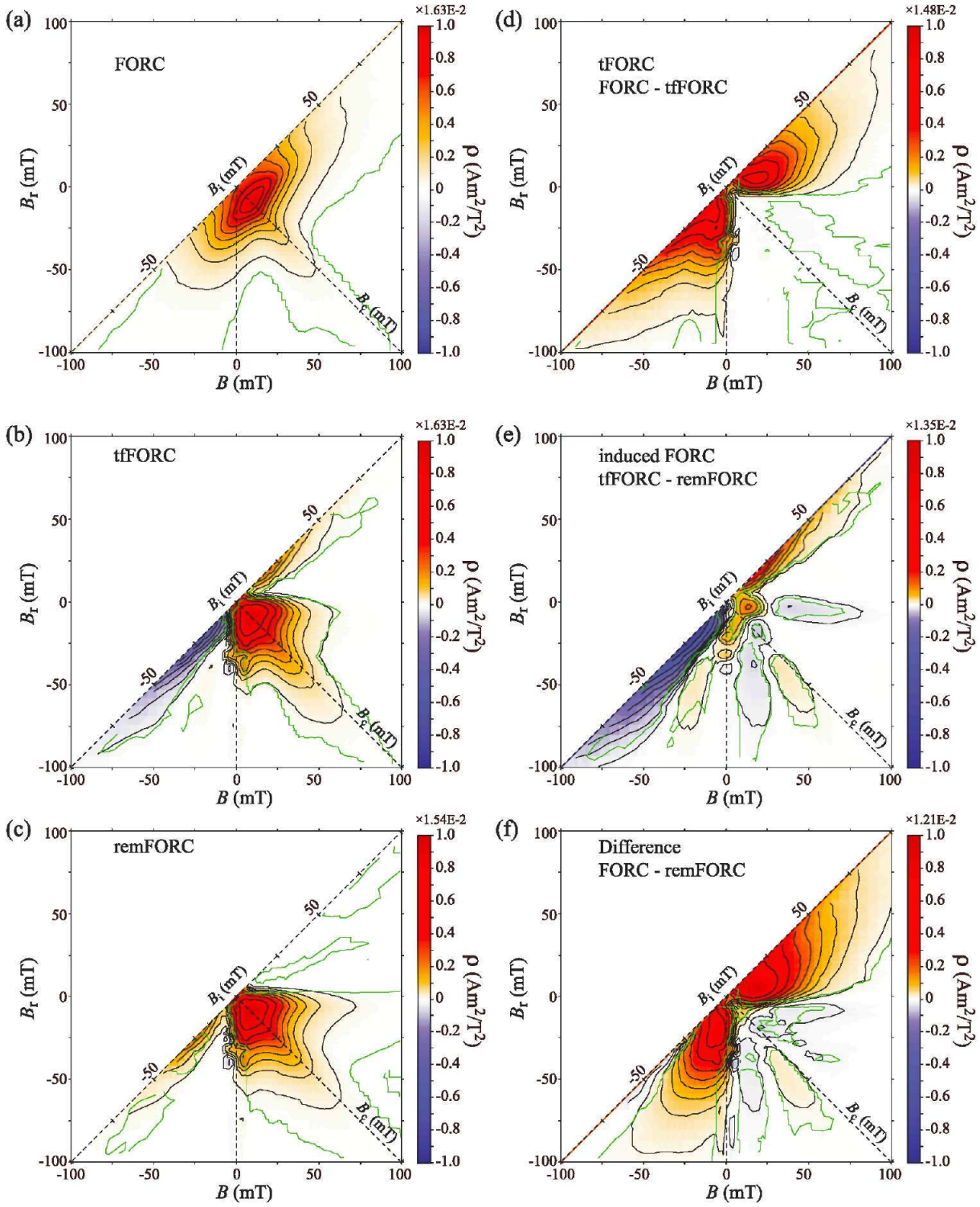

Figure 6. Sequence of six FORC diagrams for a PSD basalt sample. (a) Conventional FORC diagram, (b) tfFORC diagram, (c) remFORC diagram, (d) tFORC diagram, (e) induced FORC diagram, and (f) FORC-remFORC diagram. The green lines represent 0.05 significance levels calculated following *Heslop and Roberts* [2012]. See text for discussion.

regions, respectively (Figure 6b), which are caused by the induced magnetization (Figure 6e). In contrast, there is only one positive peak along the B_i axis in the remFORC diagram (Figure 6c), which appears to be related to thermal activation of fine particles. In the tFORC diagram (Figure 6d), two positive peaks occur in the upper right-hand and lower left-hand regions, respectively. The lower peak has a tail along the B_i axis and is due to

subtraction of the negative peak from the tfFORC diagram. The difference between the FORC and remFORC diagrams (Figure 6f) involves responses due to the tFORC, induced FORC (Figure 6e), and thermal activation effects, so that it has two opposing strong positive peaks and a slight negative peak along the lower B_i axis.

The conventional FORC diagram in Figure 6a is typical of geological "PSD" materials [e.g., *Roberts et al.*, 2000; *Muxworthy and Dunlop*, 2002; *Roberts et al.*, 2014]. However, when using the additional types of FORC diagrams presented here, positive peaks become apparent in the tFORC and FORC-remFORC diagrams above and below the $B_i = 0$ line (Figures 6d and 6f). To further explore these features, we analyzed hexagonal magnetite platelets with dimensions of several hundred nanometers across, which were produced by thermophilic iron-reducing bacteria in the laboratory [*Li*, 2012]. The magnetite has a narrow particle size range in which vortex [*Pike and Fernandez*, 1999] and noninteracting stable SD behavior are evident in a conventional room temperature FORC diagram (Figure 7a). The full range of FORC diagrams in Figure 7 contain features that are consistent with those for the PSD andesite sample in Figure 6, but with an additional magnetically noninteracting stable SD component. As discussed below, this provides evidence that some of the magnetic behavior associated with the PSD state can be described by the vortex magnetic state.

3.3. FORC Diagrams for Multidomain (MD) Samples

A FORC diagram for a 120 μm natural MD magnetite sample (Figure 8a) has a typical nearly symmetric, widely divergent distribution along the B_i axis with a small tail on the B_c axis [*Roberts et al.*, 2000, 2014; *Pike et al.*, 2001a]. The corresponding tfFORC diagram has a negative peak on the negative B_i axis, a positive peak on the positive B_i axis, and a larger positive peak in the corner of zone 3 (Figure 8b). The respective remFORC diagram has a similar positive peak in zone 3, and a smaller positive peak along the negative B_i axis (Figure 8c). The tFORC diagram has a pair of positive peaks along the positive and negative parts of the B_i axis, respectively (Figure 8d). The induced FORC diagram (Figure 8e) has more features, with a pair of negative and positive peaks along the negative and positive B_i axis, respectively, and several negative and positive peaks in the remaining FORC space. The difference between the FORC and remFORC diagrams (Figure 8f) should have contributions from both tFORC and induced FORC features, but some contributions are suppressed by the relatively high value of the positive peak, so that this diagram is similar to the tFORC diagram in Figure 8d. The results shown in Figure 8 are typical of geological MD materials [*Roberts et al.*, 2000, 2014; *Pike et al.*, 2001a]. *Pike et al.* [2001a] presented results for electrical transformer steel; results for a similar material (silicon transformer steel) are shown in Figure 9. Compared to results for geological MD materials (Figure 8), the FORC diagrams for transformer steel (Figure 9) have lower coercivity and a more vertical distribution. Such results have been reported only once so far for geological materials [*Church et al.*, 2011].

4. Discussion

4.1. What Do FORCs Actually Measure?

The traditional FORC diagram [*Pike et al.*, 1999; *Roberts et al.*, 2000] provides a measure of remanent, induced, and transient hysteretic magnetizations, as well as thermal activation effects. The six types of FORC diagram discussed here provide information about different magnetization processes, which enables the conventional FORC diagram to be taken apart to better understand individual magnetic components. The remFORC diagram provides a measure of only the irreversible magnetization, plus any thermal activation effects, and as with the classical *Preisach* [1935] diagram, it cannot have negative regions. The tfFORC diagram provides a measure of the irreversible magnetization, the induced magnetization without transient hysteresis, and thermal activation. Transient hysteretic components contribute most of the information in zones 1 and 2 of FORC and tFORC diagrams (see Figure 2d). Zone 1 of a tFORC diagram is purely a map of transient hysteresis with little contribution from thermal activation, while zone 3 is more complex because thermal activation effects are more strongly manifested in this zone, which means that thermal effects in the two regions are not exactly the same. Overall, however, the tFORC diagram provides details of transient hysteresis. We discuss in more detail below the rich magnetic information that can be derived from the range of FORC measurements discussed. We start by discussing transient hysteresis.

4.2. What Does Transient Hysteresis Indicate?

Magnetic vortex states have a nucleation field at which the flower state disappears and the vortex state forms, and an annihilation field at which the vortex state disappears [e.g., *Schabes and Bertram*, 1988;

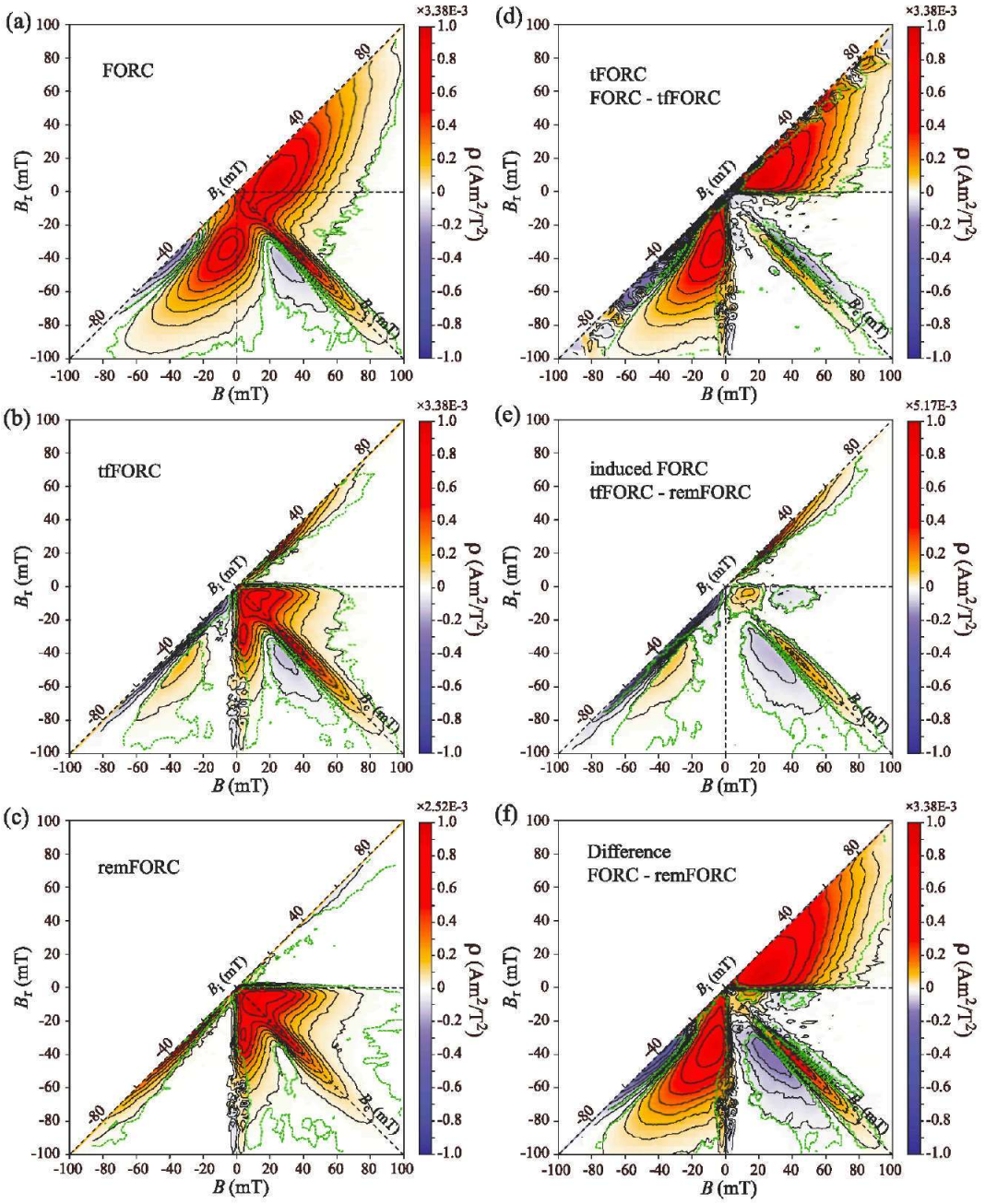

Figure 7. Sequence of six FORC diagrams for hexagonal magnetite platelets up to several hundred nanometers across [*Li*, 2012]. (a) Conventional FORC diagram, (b) tfFORC diagram, (c) remFORC diagram, (d) tFORC diagram, (e) induced FORC diagram, and (f) FORC-remFORC diagram. The green dashed lines represent 0.05 significance levels calculated following *Heslop and Roberts* [2012]. See text for discussion.

Pike and Fernandez, 1999]. For well-defined synthetic samples such as nanodotsornanowires, nucleationand annihilation fields are defined precisely, and characteristic vortex behavior is clearly evident in FORC diagrams [e.g., *Pike and Fernandez,* 1999; *Dumas et al.,* 2007a, 2007b; *Proenca et al.,* 2013]. Natural geological samples typically have broad grain size distributions, so vortex nucleation and annihilation fields will have a distribution of values, rather than a single value. By separating the contributions from different types of magnetization, it becomes apparent that transient hysteresis in a tFORC diagram (Figures 6d and 7d) provides a measure of the distributions of nucleation and annihilation fields in

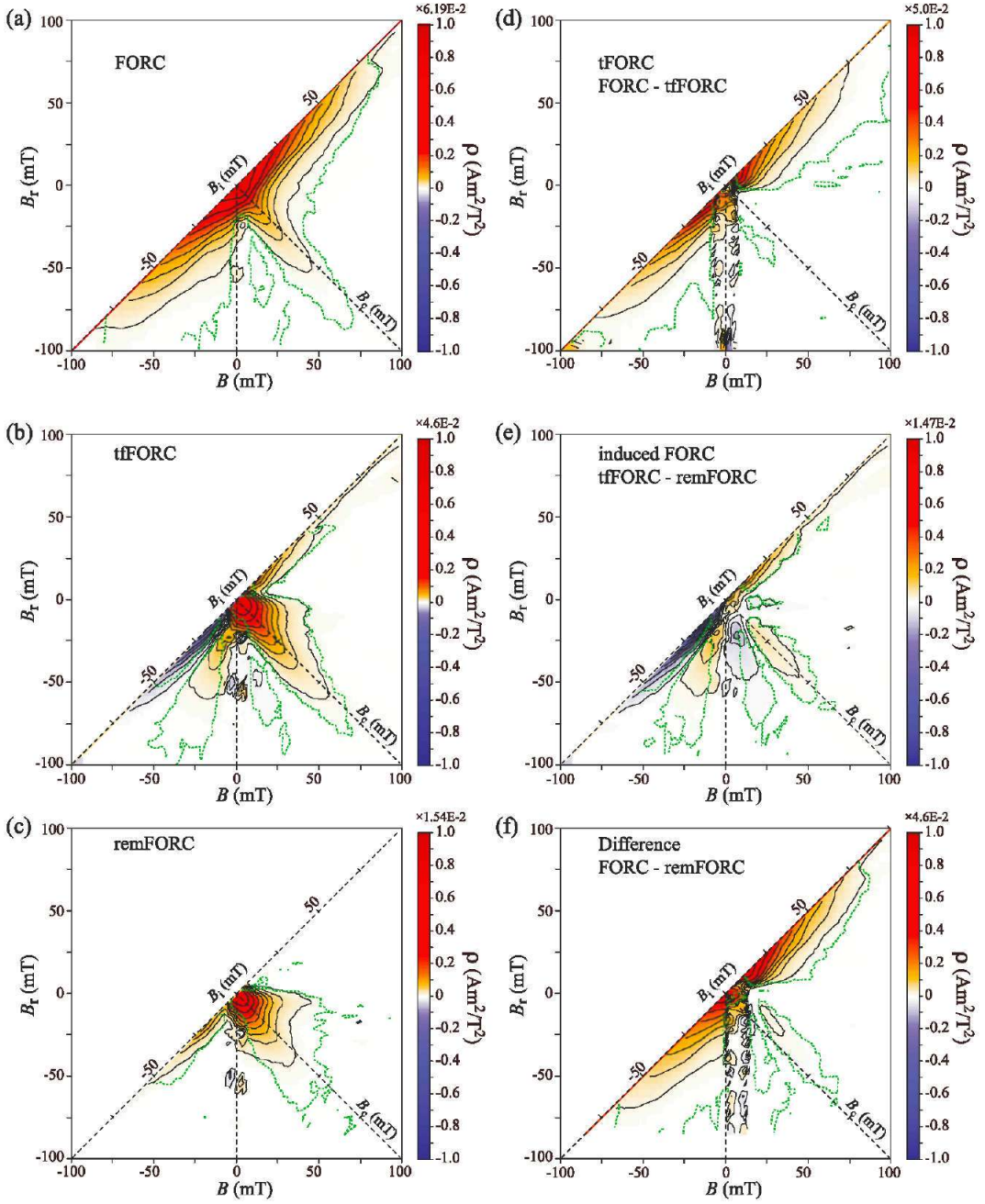

Figure 8. Sequence of six FORC diagrams for a 120 μm natural MD magnetite sample. (a) Conventional FORC diagram, (b) tfFORC diagram, (c) remFORC diagram, (d) tFORC diagram, (e) induced FORC diagram, and (f) FORC-remFORC diagram. The green dashed lines represent 0.05 significance levels calculated following *Heslop and Roberts* [2012]. See text for discussion.

contrast to the typical PSD FORC result in Figure 6a in which the presence of the magnetic vortex state is much less obvious than in Figure 7a. Vortex nucleation fields are normally smaller than annihilation fields, and both decrease with increasing grain size *[Novosad et al.,* 2001; *Dumas et al.,* 2007a, 2007b]. The positions of the positive peaks in zones 1 and 2 of a tFORC diagram (Figures 6d and 7d) provide a direct indication of the presence of the vortex domain state *[Pike and Fernandez,* 1999]; determination of vortex nucleation and annihilation fields for groups of samples will provide a measure of relative grain size variations. As the elongated concentric tFORC distribution (e.g., Figures 6d and 7d) shrinks to lower field values with increasing particle size, domain walls will eventually nucleate and MD behavior will become

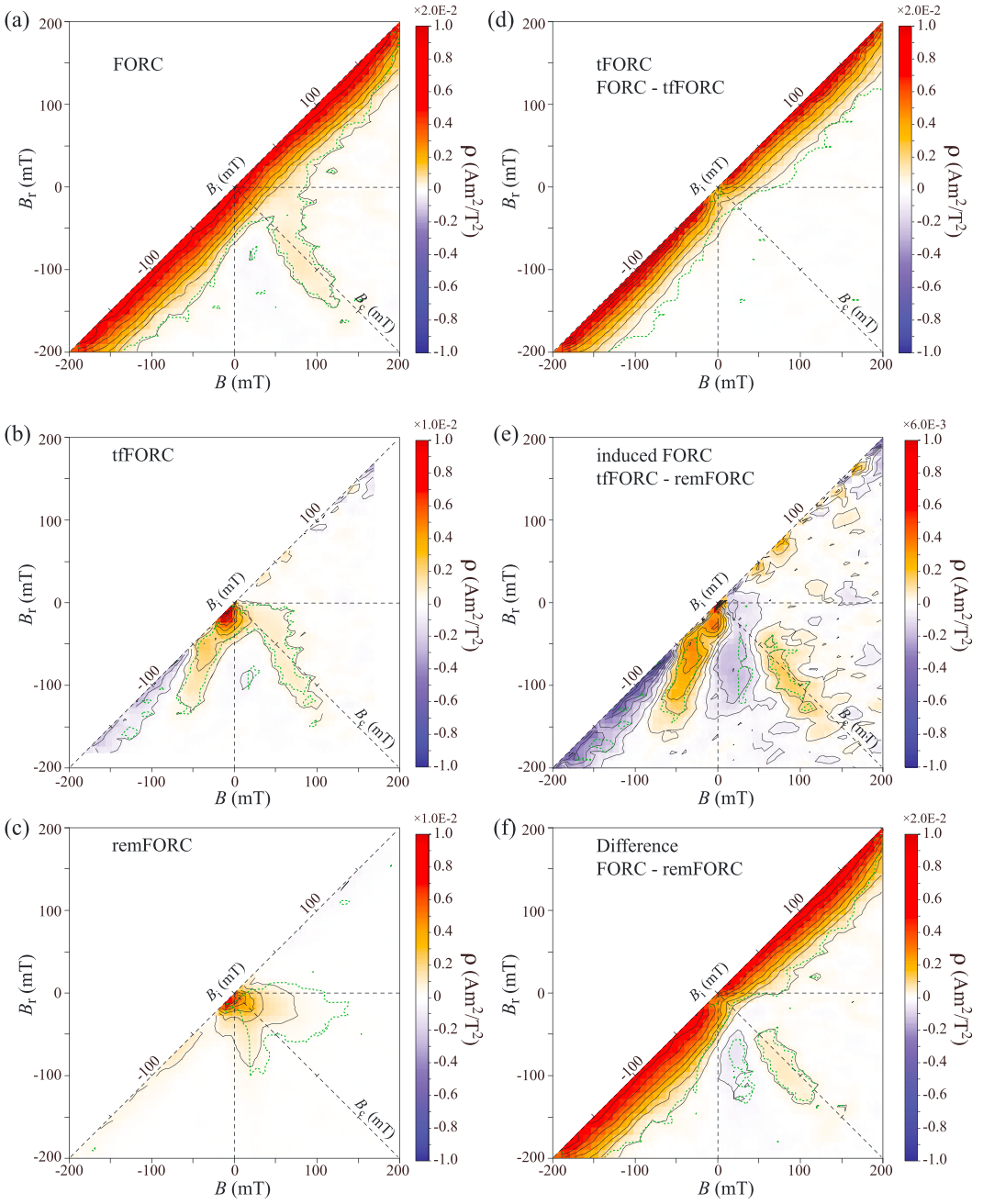

Figure 9. Sequence of six FORC diagrams for a MD silicon steel sample. (a) Conventional FORC diagram, (b) tfFORC diagram, (c) remFORC diagram, (d) tFORC diagram, (e) induced FORC diagram, and (f) FORC-remFORC diagram. The green dashed lines represent 0.05 significance levels calculated following *Heslop and Roberts* [2012]. See text for discussion.

evident (e.g., Figure 8d). It is not yet clear how easy it is to separate MD behavior from larger vortex states, but it is clear that increasing grain size will decrease the nucleation and annihilation fields. Additionally, transient hysteresis is evident in the tFORC diagrams in Figures 4d and 5d, which seems contrary to the expectation that only stable SD particles should be present in a commercially developed magnetic recording medium (Figure 4). However, with grain size or shape variations (e.g., changes in aspect ratio), magnetic behavior can change from a SD to a vortex state. The extent of such changes in hysteresis behavior depends on the degree to which particle size and shape have changed [e.g., *Cowburn et al.*, 1999]. Particle size distributions, thus, appear to have extended into the range with transient hysteresis effects (Figures 4 and 5).

4.3. Nucleation Model for a Natural MD Sample

When a particle in the magnetic vortex state becomes sufficiently large, vortex nucleation and annihilation fields will be small. At a certain particle size, domain walls will nucleate and will either be pinned at certain sites or will be driven by an applied field through the particle until they are annihilated. *Pike et al.* [2001a] concluded that the domain wall pinning model of *Néel* [1955] can describe the magnetic behavior of annealed samples, but that it is not suitable for describing hysteresis data for natural MD samples. Our measurements can potentially explain natural MD FORC behavior via the nucleation and annihilation model discussed by *Pike et al.* [2001a]. The conventional FORC distribution for a natural MD sample diverges toward both the positive and negative B_i axis (Figure 8a), and both peaks in zones 1 and 2 of Figure 8d approach the origin of the FORC diagram. *Novosad et al.* [2001] demonstrated that nucleation and annihilation fields decrease with increasing size of vortex state particles. When the particle is large enough to form a domain wall, the vortex is replaced by a MD structure. Both vortex and MD structures are caused by self-demagnetization energy that drives the magnetic structure toward a minimum energy state. Thus, the two wings in tFORC diagrams (e.g., Figure 8d) that represent transient hysteresis effects can also be explained by domain wall nucleation and annihilation [*Pike et al.*, 2001a]. MD particles have little hysteresis, so that transient hysteresis is invisible in hysteresis loops. In contrast, tFORC measurements provide a useful means with which to illustrate the small nucleation and annihilation field distributions of natural MD samples. These fields are represented by the peak of the tFORC distribution at weak fields above and below $B_r = 0$ in zones 1 and 2 (Figure 8d).

4.4. Domain State Signatures

4.4.1. Superparamagnetism

Superparamagnetic (SP) particles are too small to carry a stable remanent magnetization, but they have a strong induced magnetization because their moments align easily with an external field. The magnetization of a collection of SP particles will decay gradually toward zero with a certain time rate. Frequency-dependent magnetic susceptibility, and time- and temperature-dependent isothermal remanent magnetization (IRM) measurements can be used to identify SP particles. These particles are affected by thermal activation, which makes them magnetically less stable than particles with other domain states. Detailed FORC measurements provide an inherent advantage in detecting SP signals for particles near the SP to stable SD threshold size [*Pike et al.*, 2001b]. The tFORC and especially the remFORC diagrams introduced here are particularly useful for isolating SP signals. For example, remFORC diagrams in Figures 4c and 6c provide evidence of SP particles in both the floppy disk and andesite samples. This result is confirmed by temperature-dependent magnetic susceptibility measurements [*Néel*, 1949; *Egli*, 2009; *Hrouda et al.*, 2013; *Kumari et al.*, 2015]; more details can be found in the supporting information. However, our primary focus is on remanence-bearing particles, so we do not discuss thermal activation of SP particles further.

4.4.2. Stable SD Behavior

SD particles should have no transient hysteresis [*Yu and Tauxe*, 2005], so their remFORC diagrams are similar to FORC and tfFORC diagrams, except for the lack of a negative peak in zone 2 of the remFORC diagram (e.g., Figures 4a–4c). For our floppy disk sample, the clear positive peak in zone 3 of the FORC diagram and the negative region in zone 2 indicate the dominance of uniaxial SD particles (Figure 4a). Likewise, closed contours in the main positive part of the FORC distribution in zone 3 of the tfFORC and remFORC diagrams (Figures 4b and 4c) are key indicators of the presence of SD particles. In the induced FORC diagram (Figure 4e), the negative-positive-negative triple peak feature caused by the apparent reversible magnetization [*Della Torre*, 1999] also provides unique evidence for the presence of stable SD particles, as explained below.

Features in FORC diagrams for materials with different domain states, such as the triple peak feature in the induced FORC diagram for SD particles (Figure 4e), can be explained visually by considering the hysteresis response of different types of magnetic particles. *Stoner and Wohlfarth* [1948] produced a simple and elegant model of magnetic hysteresis behavior, which is useful for exploring how different types of fine magnetic particle contribute to a FORC distribution. In this model, a square hysteresis loop results when a magnetic field is applied parallel to the easy axis of magnetization for an isolated uniaxial SD particle (dark blue in Figure 10a). The shoulders of the loop become more rounded as the angle between the easy axis and the field increases (5°–45° in Figure 10a), until the loop collapses and becomes completely reversible when the field is applied 90° to the easy axis (green in Figure 10a). In the classical *Preisach* [1935] model, square hysterons (Figure 10b) are used to visualize the FORC response [e.g., *Roberts et al.*, 2000, 2014]. In this conceptualization, a single

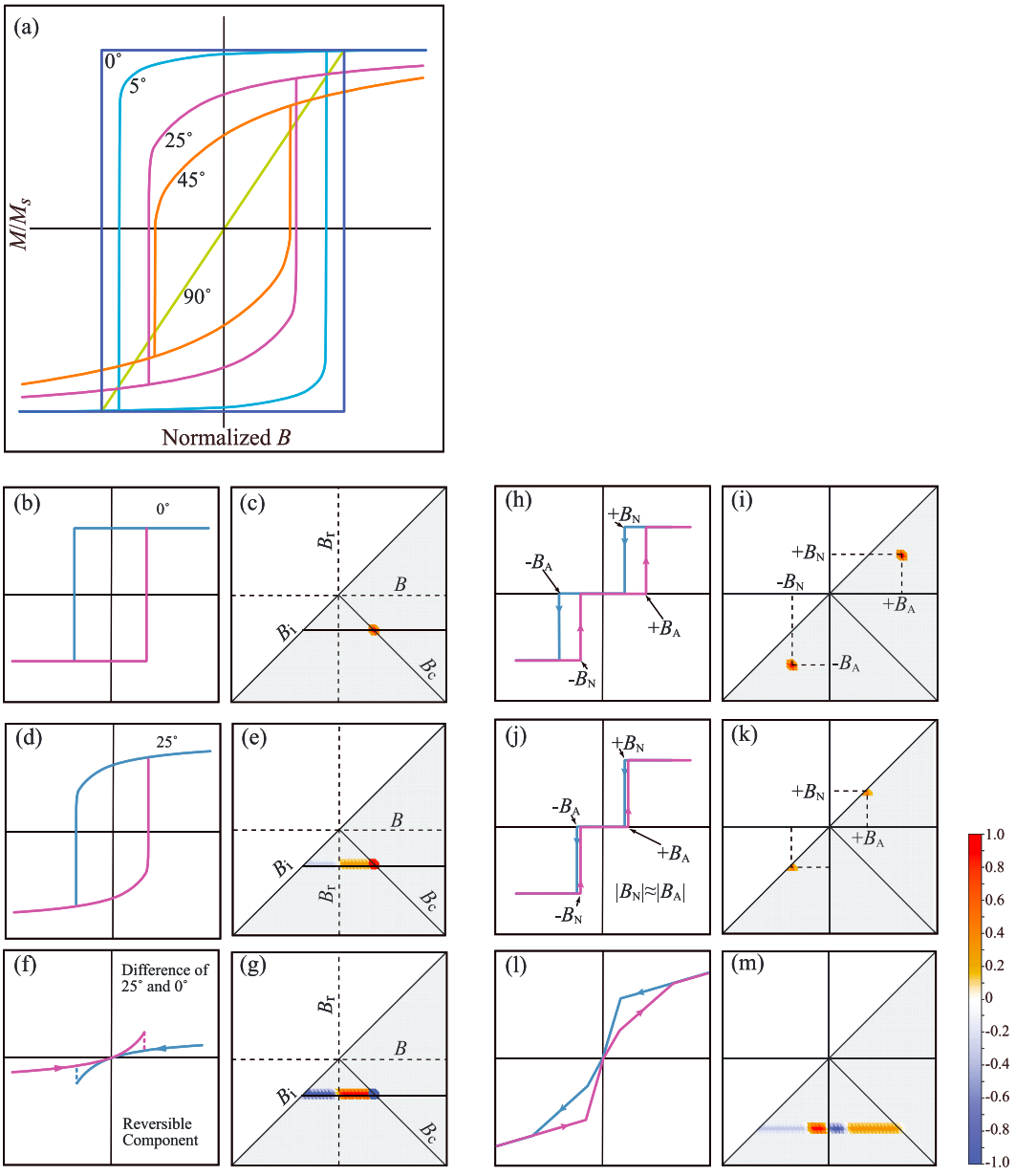

Figure 10. Schematic illustration of magnetization mechanisms and their contributions to FORC distributions. (a) Illustration of hysteresis loops for stable SD particles with easy axes at different angles with respect to the applied field (from *Stoner and Wohlfarth* [1948]). (b) Hysteron for an isolated SD particle with easy axis parallel to the applied field, as used in the Classical Preisach model (CPM) of *Preisach* [1935], and (c) its response on a FORC diagram. (d) Hysteresis loop for a Stoner-Wohlfarth particle oriented 25° to the applied field direction, and (e) its nonsingular response with strong positive and weak negative regions on a FORC diagram. For a detailed explanation of this response, see *Muxworthy et al.* [2004], *Newell* [2005], or *Roberts et al.* [2014]. (f) Illustration of the reversible component of magnetization obtained by subtracting the loop in Figure 10b from that in Figure 10d following *Della Torre* [1999]. (g) The FORC response due to calculation of the mixed second derivative (equation (1)) of the reversible component in Figure 10f, which gives rise to a negative-positive-negative triple peak response. (h) Split hysteron representation for a magnetic vortex state (following *Pike and Fernandez* [1999], where B_N is the vortex nucleation field and B_A is the annihilation field. (i) The FORC diagram for such a split hysteron has a positive peak in both the upper and lower FORC half planes, where the distance of the peaks from the B_c axis is a measure of the strength of B_N and B_A, and their distance from the B_i axis is a measure of the coercivity (width of the hysteron), as is also illustrated for (j and k) a coarser-grained lower coercivity vortex state. When domain walls start to nucleate in a vortex state particle, an induced magnetization will also be present so that the (l) mixed second derivative (equation (1)) of the reversible component gives rise to a (m) negative-positive-negative-positive response. See text for a more detailed discussion.

hysteron will give rise to a point response in FORC space where the *x-y* coordinates of the response correspond to the coercivity and interaction fields, respectively, of the hysteron (Figure 10c). When more realistic behavior is considered for SD Stoner-Wohlfarth particles (Figure 10d), the FORC response for a single particle is more complex. As explained by *Muxworthy et al.* [2004], *Newell* [2005], and *Roberts et al.* [2014], such particles will give rise to a negative region near the B_i axis, a main positive peak in a position that corresponds to the coercivity and interaction fields of the particle, and a weaker positive region between the negative region and the main positive peak (Figure 10e). The induced magnetization associated with Stoner-Wohlfarth particles would normally be thought to be completely reversible and would therefore be expected to disappear when the second derivative is calculated to determine a FORC distribution (equation (1)). However, as illustrated in Figure 10f, the difference between a square hysteron (Figure 10b) and a Stoner-Wohlfarth loop for a SD particle oriented 25° to the field (Figure 10d) gives rise to a small remaining induced magnetization as illustrated by *Della Torre* [1999, p. 56], which he called the apparent reversible magnetization (Figure 10f). This component will give rise to a weak response in an induced FORC diagram, where curvature of the magnetization curves in Figure 10f gives rise to a negative-positive-negative triple peak, as mentioned above (Figure 10g). It is this signature, which is associated with the change of induced magnetizations, that gives rise to the observed triple peak in induced FORC diagrams [*Bodale et al.*, 2011] for SD materials in Figures 4e and 5e.

4.4.3. Vortex and MD States

As discussed above, transient hysteresis is the main feature associated with the vortex and MD states. Information in zone 1 of a FORC diagram indicates the existence of transient hysteresis because SD behavior does not give rise to a response in FORCs on and above the zero-FORC (see definition in Figures 2c and 2d). The two positive regions in zones 1 and 2 of a tFORC diagram (Figures 6d and 7d) are unique characteristics of a vortex structure; a butterfly-shaped pattern can be observed in zone 3 of a tFORC diagram if a sample has different vortex nucleation and annihilation fields [*Pike and Fernandez*, 1999]. This feature is usually invisible, however, because it is obscured by its relative weakness compared with the main FORC response associated with the vortex state (Figure 6d). The peak in zone 1 (Figure 6d) is clearer than that in zone 2 because zone 1 is negligibly influenced by thermal fluctuations and its response is closer to magnetic saturation. The tfFORC and remFORC diagrams have a clear SD-like peak with low coercivity (Figures 6b and 6c). Transient hysteresis is also useful for understanding MD materials. The conventional FORC distribution for a natural MD sample diverges toward both the positive and negative B_i axis (Figure 8a). The two wings in the tFORC diagram (Figure 8d) represent transient hysteresis effects that indicate domain wall nucleation and annihilation field distributions [*Pike et al.*, 2001a].

The *Stoner and Wohlfarth* [1948] model is only suitable for describing SD particle systems. The hysteresis behavior associated with the magnetic vortex state is often described using simplified hysteron-like loops [e.g., *Pike and Fernandez*, 1999] (Figure 10h) or modifications thereof [e.g., *Dumas et al.*, 2007b] that are split into two parts at vortex nucleation B_N and annihilation B_A fields. In a simple representation with hysteron-like loops, the vortex state gives rise to positive peaks in both zones 1 and 2 of a FORC diagram (Figure 10i). As particle size increases, the difference between B_N and B_A decreases (Figure 10j) and the positive upper and lower peaks move toward both the B_i and B_c axes of a FORC diagram (Figure 10k). These types of features are clearly evident in the tFORC diagram for the studied andesite sample (Figure 6d).

When domain walls start to nucleate, most of the FORC, tFORC, and FORC-remFORC distributions have low coercivities and align almost parallel to the B_i axis (e.g., Figure 8). The induced FORC diagram is more complex (Figure 8e) and has a negative-positive-negative-positive pattern that is also observed for vortex state samples (Figures 6e and 7e). The induced magnetization depends on the total magnetization, which depends on the applied external field strength and magnetization state. Vortex and MD samples can be approximated by a goose-necked hysteresis loop (Figure 10l), as observed in micromagnetic simulations [*Goiriena-Goikoetxea et al.*, 2016], which produces the negative-positive-negative-positive pattern observed in FORC diagrams (Figure 10m). We do not have a detailed physical interpretation for this behavior; we simply point to it as needing explanation.

4.5. The Preisach Model

As discussed above, hysteresis loops are generalized as simplified square hysterons in the *Preisach* [1935] model of hysteresis. The *Preisach* [1935] model is effectively a probability density distribution of hysterons

with distributed switching and interaction fields; integration over the whole Preisach distribution should give the saturation magnetization. Based on this requirement, only the remFORC diagram approximates a Preisach distribution if thermal activation in zone 3 is negligible. *Dunlop et al.* [1990] considered zone 3 as the only region where the remanent state will produce a signal and defined this region as the Preisach space. *Carvallo et al.* [2005] compared FORC and remanent Preisach diagrams and concluded that they are equivalent at some level; however, there are significant differences between FORCs and remFORCs upon closer inspection (Figures 4–9). The differences are associated with contributions from induced magnetizations that affect both interaction fields and coercivity. In the classical Preisach model (CPM), the FORC distribution is the product of the independent interaction field and coercivity distributions [*Néel*, 1954]. However, with independent integrals for the interaction field and coercivity distributions, a slightly different remFORC distribution will be created. This means that the CPM is not well suited to describing hysteresis in natural samples; a moving Preisach model [*Vajda and Della Torre*, 1991] has therefore been argued to be more applicable [*Pike et al.*, 1999]. Generally, zone 3 in a remFORC diagram is equivalent to a Preisach distribution, where integration over the distribution gives the saturation remanent magnetization. The remFORC diagram is not only a probability distribution of elemental hysterons, but it also defines the relationship between interaction fields and coercivity that controls the pattern of the FORC distribution. A remFORC distribution is controlled by the magnetic mineralogy, the grain size of the constituent magnetic minerals, the packing fraction of magnetic grains, and the magnetic anisotropy.

Generally, vertical profiles in rotated FORC diagrams are considered to represent interaction field distributions at a given B_c value, and horizontal profiles represent coercivity distributions [*Pike et al.*, 1999; *Muxworthy and Williams*, 2005; *Egli*, 2006; *Winklhofer and Zimanyi*, 2006; *Dobrota and Stancu*, 2013]. Transient hysteresis contributes to FORC distributions but not to the saturation (or remanent) magnetization of samples that contain coarse magnetic particles. The influence of transient hysteresis is therefore removed in tfFORC and remFORC diagrams, so that zone 3 in these diagrams represents the true coercivity and interaction field distributions. Coercivity distributions obtained from IRM acquisition curves or FORC central ridge profiles along the B_c axis are good approximations but do not represent the true bulk coercivity distribution, even though coercivity values correlate well [*Li et al.*, 2012; *Roberts et al.*, 2012]. FORC and tfFORC diagrams are not equivalent to a Preisach diagram because of their lack of symmetry and the possible presence of negative regions in these diagrams. In contrast, remFORC distributions do not contain negative regions and are more symmetrical and more closely represent Preisach distributions. SP particles contribute to a remFORC distribution, so we only consider zone 3 of a remFORC diagram to represent a Preisach distribution.

The Preisach distribution is the product of two independent distributions: the interaction field and the coercivity distributions [*Dunlop et al.*, 1990], which can be calculated by integrating the remFORC distribution along the B_i and B_c axes, respectively. The profile along the B_c axis is the coercivity distribution with zero interaction rather than the bulk coercivity distribution. In contrast, a vertical profile at any B_c value is the interaction field distribution at that coercivity value. Independent interaction field and coercivity distributions for a floppy disk sample are shown in Figure 11. The interaction field distribution is calculated from the remFORC diagram, which represents purely the effect of interactions on the remanent magnetization (grey line, Figure 11a), while that calculated from the tfFORC diagram includes contributions from the induced magnetization (green line, Figure 11a). The difference between the two (pink line, Figure 11a) indicates that the interaction field distribution is shifted toward negative values due to the induced magnetization. The remanence coercivity distribution is plotted in Figure 11b, where the red and grey dots represent the distribution calculated from IRM acquisition and DC demagnetization curves [*Kruiver et al.*, 2001; *Egli*, 2003], respectively, and the grey and green lines represent distributions integrated from the remFORC and tfFORC diagrams, respectively. Coercivity distributions calculated from IRM acquisition and DC demagnetization curves are affected by magnetostatic interactions [*Muxworthy et al.*, 2004], while those integrated from the remFORC diagram represent the intrinsic switching field distribution. For the studied floppy disk sample, the induced magnetization shifts the remanence coercivity distribution to smaller values (pink line, Figure 11b). Assessment of interaction effects on the remanent magnetization is important, for example, in assessing absolute paleointensity results [e.g., *Carvallo et al.*, 2006b; *Paterson et al.*, 2010]. The approach demonstrated in Figure 11 from remFORC diagrams can assist with assessing this important factor. Similarly, our new types of FORC diagram may be useful for the FORC-based paleointensity method [*Muxworthy and Heslop*, 2011; *Muxworthy et al.*, 2011]. The FORC paleointensity method uses zone 3 of a conventional FORC diagram to simulate remanence

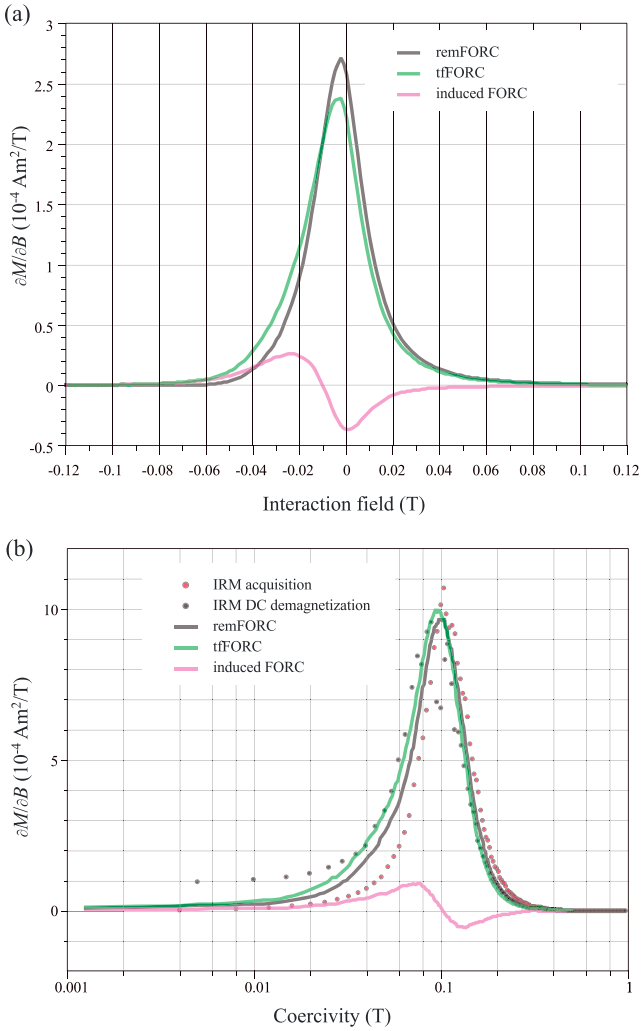

Figure 11. Interaction field and coercivity distributions for a stable SD floppy disk sample calculated from the remFORC diagram in Figure 4c. These distributions represent purely the effect of interactions on (a) the remanent magnetization (grey line), while those calculated from the tfFORC diagram include induced magnetization contributions (green line). The difference between the two is given by the pink line, which indicates a shift of the entire FORC distribution to negative values due to the induced magnetization. (b) The remanence coercivity distribution calculated from different data sets. The red and grey dots are from IRM acquisition and DC demagnetization curves, respectively; the grey and green lines are from integration with respect to B_i over the remFORC and tfFORC space, respectively, while the pink line represents the difference between them (due to the induced magnetization).

recording ability by assuming that the FORC distribution approximates a Preisach distribution. However, as we have illustrated, this region of a conventional FORC diagram contains contributions from both remanent and induced components, which can invalidate the Preisach assumption. Use of remFORC diagrams could be more appropriate and may provide an improved means of obtaining FORC-based paleointensity estimates.

4.6. The Importance of Adjustable Nonlinear Color Scales

We note that visualizing information on FORC diagrams depends on the color scale used. FORC diagrams are often plotted with a linear gray scale or color scale. Available colors must represent the full range of values in a FORC distribution; few colors can be devoted to relatively narrowly clustered values of interest, so detail is usually lost. Even specially designed color scales (e.g., the saturated color scale of *Egli* [2013]) do not enable completely unbiased interpretation in some cases. If such detail is important, then something must be done to bring it out. The idea behind the use of adjustable nonlinear color scales is to distort the color scale such that more colors are applied to the region of interest and fewer colors are applied elsewhere. Positive and negative FORC distribution values normally both occur, so a symmetric transformation function (e.g., a hyperbolic tangent function or even the familiar inclination error formula [*King*, 1955]) can be used to change the apparent importance of positive and negative parts of a FORC distribution while keeping a constant color for the zero value. Information carried by low values of a FORC distribution is easily hidden with a normal color scale [*Keahey and Robertson*, 1996], so we illustrate the value of nonlinear color scales in two ways. One is to illustrate contributions from hematite, which has a relatively low magnetization and that produces a signal over a relatively large area of a FORC diagram, which makes its contribution difficult to detect when it cooccurs with strongly magnetized minerals such as magnetite (Figures 12c and 12d). In such situations, expression of the weakly magnetized material is suppressed (Figure 12c), which makes it invisible in conventional FORC diagrams [e.g., *Muxworthy et al.*, 2005; *Roberts et al.*, 2014]. With a nonlinear color scale with user control, the signal due to a weakly magnetized high coercivity component can become much clearer (Figure 12d).

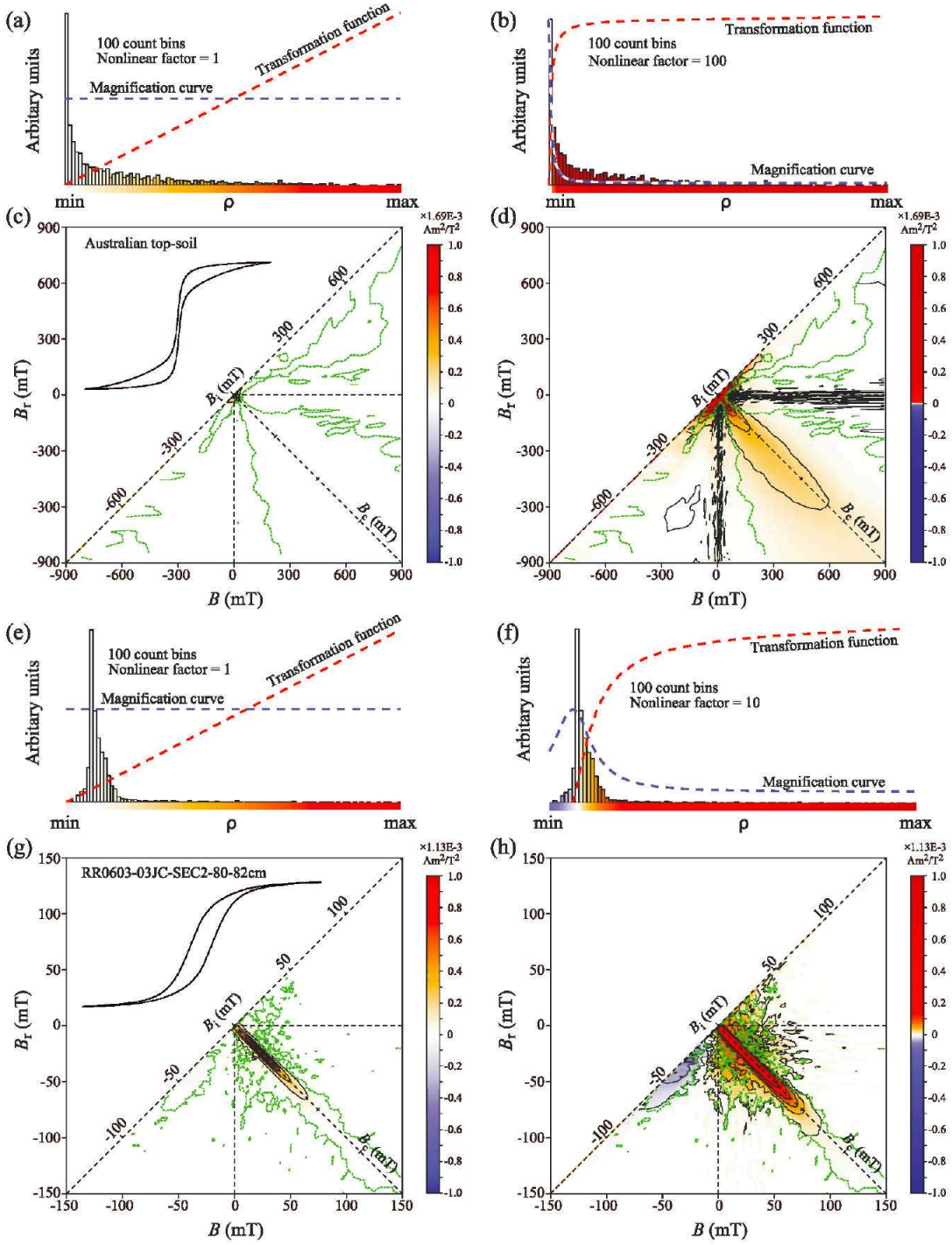

Figure 12. Illustration of the importance of nonlinear color scales for identifying contributions from weakly magnetized components in FORC diagrams. (a and b) Histograms of ρ values with 100 count bins for the (c and d) FORC diagrams, respectively, where the red dashed lines represent the nonlinear transformation function. A straight-line transformation function (nonlinear factor = 1) gives a linear color scale (Figure 12a), and a curved function represents a nonlinear color scale (Figure 12b), where the nonlinear factor quantifies the nonlinearity (which varies with the transformation function selected). The blue dashed lines are magnification curves that indicate the color scale magnification and are the derivative of the transformation function. FORC diagrams for a linear (Figure 12c) and user-selected nonlinear (Figure 12d) color scale for a sample with mixed PSD magnetite and stable SD hematite. A hematite component is invisible in Figure 12c but is identified clearly with the nonlinear color scale in Figure 12d. (e and f) Histograms of the FORC distributions with (g) linear and (h) nonlinear color scales for a pelagic marine sediment from the eastern equatorial Pacific Ocean (sample RR0603-03JC-SEC2-80-82cm [*Chang et al.*, 2016]) that contains a dominant noninteracting stable SD contribution. This contribution is the only component evident in Figure 12g, whereas an additional interacting SD contribution is evident in the nonlinear color scale in Figure 12h. Use of nonlinear color scales in these cases avoids the diagnostic issues mentioned by *Muxworthy et al.* [2005] and *Roberts et al.* [2014] in relation to mixed FORC distributions with strong and weak components. The insets in Figures 12c and 12e are the respective major hysteresis loops for each sample.

In Figures 12c and 12d, the dominant low coercivity component is due to a detrital PSD magnetite, and the high coercivity component is due to hematite, which makes a weak contribution over a large area of the FORC diagram. The presence of hematite is obvious from the major hysteresis loop (inset in Figure 12c), from IRM acquisition curves, or from the remFORC diagram. Another example involves an interacting detrital SD component that cooccurs with a biogenic magnetite component (sample RR0603-03JC-SEC2-80-82cm [*Chang et al.*, 2016]). The detrital interacting SD component has a suppressed signal with respect to the dominant noninteracting biogenic component (Figures 12g and 12h). A histogram of FORC values is helpful for selecting a suitable nonlinear factor (Figures 12a, 12b, 12e, and 12f), where a nonlinear factor of 1 represents a linear color scale. The magnification curve is the derivative of the transformation function and helps a user to decide which information to emphasize (Figure 12). Use of a nonlinear color scale makes these weak signals much clearer and changes the question when interpreting such FORC diagrams from whether a magnetic component is evident to how much of the component is present. This is fundamentally important in many paleomagnetic and environmental magnetic uses of FORC diagrams. Nonlinear color scales provide an effective means of bringing the full level of information sought from FORC diagrams within reach of meaningful interpretation—with quantified statistical significance levels following *Heslop and Roberts* [2012].

5. Conclusions

FORC diagrams provide powerful and detailed information about switching and interaction field distributions, and about hysteresis mechanisms [*Roberts et al.*, 2014]. We outline an approach that involves experimental measurement of three sets of FORC data from which we present six types of FORC distribution. The combined information carried by these FORC diagrams provides much greater detail about magnetization processes compared to the conventional FORC diagram and adds considerable interpretive power. Remanent magnetizations, induced magnetizations, and transient hysteretic magnetizations all contribute to a conventional FORC diagram. Signals due to each of these types of magnetization and domain state signatures can now be discriminated from each other so that their contributions can be identified in different types of FORC diagrams. This approach provides a much clearer framework for interpreting FORC diagrams.

Identification of transient hysteresis magnetization contributions makes it easier to identify vortex or MD magnetic states. Even though it remains difficult to distinguish MD states from vortex states with weak nucleation/annihilation fields, estimation of vortex and domain nucleation and annihilation fields from a transient FORC diagram provides an indicator of particle size because there is a negative correlation between nucleation field and particle size. Transient-free FORC and especially remFORC diagrams are useful for detecting SP particles. Zone 3 of a remFORC diagram can be considered as similar to the *Néel* [1954] interpretation of a *Preisach* [1935] distribution, in that it enables quantification of coercivity and interaction field distributions for the remanent magnetization, which has powerful implications for assessing the influence of magnetostatic interactions on paleomagnetic recording (which is especially important for paleointensity analysis). Compared to the vortex and MD states, SD samples have a stronger induced magnetization that is evident in induced FORC distributions.

While determination of six types of FORC diagram is more time-consuming than for a conventional set of FORC measurements, the interpretive value of the additional information provided is considerable. The fingerprints of different domain states that can be unlocked by the additional information provided by the six types of FORC diagram discussed here should enable more rigorous interpretation of FORC diagrams. The approach outlined here should also contribute to development of more quantitative interpretation of FORC diagrams.

Acknowledgments
This work was supported by the Australian Research Council (grant DP160100805) and the National Natural Science Foundation of China (grants 41522402, 41374004, 41374072, and 41574063). The software for processing the six types of FORC diagram presented here is available from https://sites.google.com/site/irregularforc/. We thank Brad Pillans, Lizzie Ingham, Pengxiang Hu, and the Oregon State University Marine Geology Repository (supported by NSF grant OCE-1558679) for supplying samples for which results are presented in Figures 5, 6, 12a–12d, and 12e–12h, respectively. We are grateful to two anonymous reviewers for comments that improved the manuscript significantly.

References

Bodale, I., L. Stoleriu, and A. Stancu (2011), Reversible and irreversible components evaluation in hysteretic processes using first and second-order magnetization curves, *IEEE Trans. Magn.*, *47*, 192–197, doi:10.1109/TMAG.2010.2083679.

Carvallo, C., D. J. Dunlop, and Ö. Özdemir (2005), Experimental comparison of FORC and remanent Preisach diagrams, *Geophys. J. Int.*, *162*, 747–754, doi:10.1111/j.1365-246X.2005.02688.x.

Carvallo, C., and A. R. Muxworthy (2006), Low-temperature first-order reversal curve (FORC) diagrams for synthetic and natural samples, *Geochem. Geophys. Geosyst.*, *7*, Q09003, doi:10.1029/2006GC001299.

Carvallo, C., A. R. Muxworthy, and D. J. Dunlop (2006a), First-order reversal curve (FORC) diagrams of magnetic mixtures: Micromagnetic models and measurements, *Phys. Earth Planet. Inter.*, *154*, 308–322.
Carvallo, C., A. P. Roberts, R. Leonhardt, C. Laj, C. Kissel, M. Perrin, and P. Camps (2006b), Increasing the efficiency of paleointensity analyses by selection of samples using first-order reversal curve (FORC) diagrams, *J. Geophys. Res.*, *111*, B12103, doi:10.1029/2005JB004126.
Chang, L., A. P. Roberts, D. Heslop, A. Hayashida, J. H. Li, X. Zhao, W. Tian, and Q. H. Huang (2016), Widespread occurrence of silicate-hosted magnetic mineral inclusions in marine sediments and their contribution to paleomagnetic recording, *J. Geophys. Res. Solid Earth*, *121*, 8415–8431, doi:10.1002/2016JB013109.
Channell, J. E. T., R. J. Harrison, I. Lascu, I. N. McCave, F. D. Hibbert, and W. E. N. Austin (2016), Magnetic record of deglaciation using FORC-PCA, sortable-silt grain size, and magnetic excursion at 26 ka, from the Rockall trough (NE Atlantic), *Geochem. Geophys. Geosyst.*, *17*, 1823–1841, doi:10.1002/2016GC006300.
Chen, A. P., R. Egli, and B. M. Moskowitz (2007), First-order reversal curve (FORC) diagrams of natural and cultured biogenic magnetic particles, *J. Geophys. Res.*, *112*, B08S90, doi:10.1029/2006JB004575.
Cherchez, M., L. Stoleriu, and A. Stancu (2004), Interaction effects in high density magnetic particulate media, *Physica B*, *343*, 48–52, doi:10.1016/j.physb.2003.08.043.
Church, N., J. M. Feinberg, and R. Harrison (2011), Low-temperature domain wall pinning in titanomagnetite: Quantitative modeling of multidomain first-order reversal curve diagrams and AC susceptibility, *Geochem. Geophys. Geosyst.*, *12*, Q07Z27, doi:10.1029/2011GC003538.
Church, N. S., K. Fabian, and S. A. McEnroe (2016), Nonlinear Preisach maps: Detecting and characterizing separate remanent magnetic fractions in complex natural samples, *J. Geophys. Res. Solid Earth*, *121*, 8373–8395, doi:10.1002/2016JB013465.
Cowburn, R. P., D. K. Koltsov, A. O. Adeyeye, and M. E. Welland (1999), Single-domain circular nanomagnets, *Phys. Rev. Lett.*, *83*, 1042–1045, doi:10.1103/PhysRevLett.83.1042.
Della Torre, E. (1999), *Magnetic Hysteresis*, p. 215, IEEE Press, Piscataway, N. J.
Dobrota, C. I., and A. Stancu (2013), What does a first-order reversal curve diagram really mean? A study case: Array of ferromagnetic nanowires, *J. Appl. Phys.*, *113*, 043928, doi:10.1063/1.4789613.
Dumas, R. K., C. P. Li, I. V. Roshchin, I. K. Schuller, and K. Liu (2007a), Magnetic fingerprints of sub-100 nm Fe dots, *Phys. Rev. B*, *75*, 134405, doi:10.1103/PhysRevB.75.134405.
Dumas, R. K., K. Liu, C. P. Li, I. V. Roshchin, and I. K. Schuller (2007b), Temperature induced single domain-vortex state transition in sub-100 nm Fe nanodots, *Appl. Phys. Lett.*, *91*, 202501, doi:10.1063/1.2807276.
Dunlop, D. J. (1968), Experimental test of the Preisach-Néel model of interacting single domain grains, *Phys. Lett.*, *27*, 617–618, doi:10.1016/0375-9601(68)90082-0.
Dunlop, D. J., and Ö. Özdemir (1997), *Rock Magnetism: Fundamentals and Frontiers*, p. 573, Cambridge Univ. Press, Cambridge, U. K.
Dunlop, D. J., M. F. Westcott-Lewis, and M. E. Bailey (1990), Preisach diagrams and anhysteresis: Do they measure interactions?, *Phys. Earth Planet. Inter.*, *65*, 62–77, doi:10.1016/0031-9201(90)90076-A.
Egli, R. (2003), Analysis of the field dependence of remanent magnetization curves, *J. Geophys. Res.*, *108*(B2), 2081, doi:10.1029/2002JB002023.
Egli, R. (2006), Theoretical aspects of dipolar interactions and their appearance in first-order reversal curves of thermally activated single-domain particles, *J. Geophys. Res.*, *111*, B12S17, doi:10.1029/2006JB004567.
Egli, R. (2009), Magnetic susceptibility measurements as a function of temperature and frequency I: Inversion theory, *Geophys. J. Int.*, *177*, 395–420, doi:10.1111/j.1365-246X.2009.04081.x.
Egli, R. (2013), VARIFORC: An optimized protocol for calculating non-regular first-order reversal curve (FORC) diagrams, *Global Planet. Change*, *110*, 302–320, doi:10.1016/j.gloplacha.2013.08.003.
Egli, R., A. P. Chen, M. Winklhofer, K. P. Kodama, and C. S. Horng (2010), Detection of noninteracting single domain particles using first-order reversal curve diagrams, *Geochem. Geophys. Geosyst.*, *11*, Q01Z11, doi:10.1029/2009GC002916.
Ewing, J. A. (1882), On effects of retentiveness in the magnetisation of iron and steel, *Proc. R. Soc. London*, *34*, 39–45, doi:10.1098/rspl.1882.0010.
Fabian, K. (2003), Some additional parameters to estimate domain state from isothermal remanent magnetization, *Earth Planet. Sci. Lett.*, *213*, 337–345, doi:10.1016/S0012-821X(03)00329-7.
Fabian, K., and T. von Dobeneck (1997), Isothermal magnetization of samples with stable Preisach function: A survey of hysteresis, remanence, and rock magnetic parameters, *J. Geophys. Res.*, *102*, 17,659–17,677, doi:10.1029/97JB01051.
Goiriena-Goikoetxea, M., A. García-Arribas, M. Rouco, A. V. Svalov, and J. M. Barandiaran (2016), High-yield fabrication of 60 nm Permalloy nanodiscs in well-defined magnetic vortex state for biomedical applications, *Nanotechnology*, *27*, 175302, doi:10.1088/0957-4484/27/17/175302.
Harrison, R. J., and I. Lascu (2014), FORCulator: A micromagnetic tool for simulating first-order reversal curve diagrams, *Geochem. Geophys. Geosyst.*, *15*, 4671–4691, doi:10.1002/2014GC005582.
Hejda, P., and T. Zelinka (1990), Modelling of hysteresis processes in magnetic rock samples using the Preisach diagram, *Phys. Earth Planet. Inter.*, *63*, 32–40, doi:10.1016/0031-9201(90)90057-5.
Heslop, D., and A. P. Roberts (2012), Estimation of significance levels and confidence intervals for first-order reversal curve distributions, *Geochem. Geophys. Geosyst.*, *13*, Q12Z40, doi:10.1029/2012GC004115.
Heslop, D., A. P. Roberts, and L. Chang (2014), Characterizing magnetofossils from first-order reversal curve central ridge signatures, *Geochem. Geophys. Geosyst.*, *15*, 2170–2179, doi:10.1002/2014GC005291.
Hrouda, F., J. Pokorný, J. Ježek, and M. Chadima (2013), Out-of-phase magnetic susceptibility of rocks and soils: A rapid tool for magnetic granulometry, *Geophys. J. Int.*, *194*, 170–181, doi:10.1093/gji/ggt097.
Keahey, T. A., and E. L. Robertson (1996), Techniques for non-linear magnification transformations, *Proc. IEEE Symp. Inf. Visualization*, 38–45, doi:10.1109/INFVIS.1996.559214.
King, R. F. (1955), The remanent magnetism of artificially deposited sediments, *Mon. Not. R. Astron. Soc. Geophys. Suppl.*, *7*, 115–134, doi:10.1111/j.1365-246X.1955.tb06558.x.
Kruiver, P. P., M. J. Dekkers, and D. Heslop (2001), Quantification of magnetic coercivity components by the analysis of acquisition curves of isothermal remanent magnetization, *Earth Planet. Sci. Lett.*, *189*, 269–276, doi:10.1016/S0012-821X(01)00367-3.
Kumari, M., A. M. Hirt, R. Uebe, D. Schüler, É. Tompa, M. Pósfai, W. Lorenz, F. Ahrentorp, C. Jonasson, and C. Johansson (2015), Experimental mixtures of superparamagnetic and single-domain magnetite with respect to Day-Dunlop plots, *Geochem. Geophys. Geosyst.*, *16*, 1739–1752, doi:10.1002/2015GC005744.
Lappe, S.-C. L. L., N. S. Church, T. Kasama, A. Bastos da Silva Fanta, G. Bromiley, R. E. Dunin-Borkowski, J. M. Feinberg, S. Russell, and R. J. Harrison (2011), Mineral magnetism of dusty olivine: A credible recorder of pre-accretionary remanence, *Geochem. Geophys. Geosyst.*, *12*, Q12Z35, doi:10.1029/2011GC003811.

Lappe, S.-C. L. L., J. M. Feinberg, A. Muxworthy, and R. J. Harrison (2013), Comparison and calibration of nonheating paleointensity methods: A case study using dusty olivine, *Geochem. Geophys. Geosyst.*, *14*, 2143–2158, doi:10.1002/ggge.20141.

Lascu, I., R. J. Harrison, Y. Li, J. R. Muraszko, J. E. T. Channell, A. M. Piotrowski, and D. A. Hodell (2015), Magnetic unmixing of first-order reversal curve diagrams using principal component analysis, *Geochem. Geophys. Geosyst.*, *16*, 2900–2915, doi:10.1002/2015GC005909.

Li, Y. L. (2012), Hexagonal platelet-like magnetite as a biosignature of thermophilic iron-reducing bacteria and its applications to the exploration of the modern deep, hot biosphere and the emergence of iron-reducing bacteria in early Precambrian oceans, *Astrobiology*, *12*, 1100–1108, doi:10.1089/ast.2012.0847.

Li, J. H., W. F. Wu, Q. S. Liu, and Y. X. Pan (2012), Magnetic anisotropy, magnetostatic interactions and identification of magnetofossils, *Geochem. Geophys. Geosyst.*, *13*, Q10Z51, doi:10.1029/2012GC004384.

Liu, Q. S., A. P. Roberts, J. C. Larrasoaña, S. K. Banerjee, Y. Guyodo, L. Tauxe, and F. Oldfield (2012), Environmental magnetism: Principles and applications, *Rev. Geophys.*, *50*, RG4002, doi:10.1029/2012RG000393.

Mayergoyz, I. D. (1986), Mathematical models of hysteresis, *IEEE Trans. Magn.*, *22*(5), 603–608.

Muxworthy, A. R., and D. J. Dunlop (2002), First-order reversal curve (FORC) diagrams for pseudo-single-domain magnetites at high temperature, *Earth Planet. Sci. Lett.*, *203*, 369–382, doi:10.1016/S0012-821X(02)00880-4.

Muxworthy, A. R., and D. Heslop (2011), A Preisach method for estimating absolute paleofield intensity under the constraint of using only isothermal measurements: 1. Theoretical framework, *J. Geophys. Res.*, *116*, B04102, doi:10.1029/2010JB007843.

Muxworthy, A. R., D. Heslop, G. A. Paterson, and D. Michalk (2011), A Preisach method for estimating absolute paleofield intensity under the constraint of using only isothermal measurements: 2. Experimental testing, *J. Geophys. Res.*, *116*, B04103, doi:10.1029/2010JB007844.

Muxworthy, A. R., and W. Williams (2005), Magnetostatic interaction fields in first-order-reversal curve diagrams, *J. Appl. Phys.*, *97*, 063905, doi:10.1063/1.1861518.

Muxworthy, A. R., and A. P. Roberts (2007), First-order reversal curve (FORC) diagrams, in *Encyclopedia of Geomagnetism and Paleomagnetism*, *Encycl. Earth Sci. Ser.*, edited by D. Gubbins and E. Herrero-Bervera, pp. 266–272, Springer, Dordrecht, Netherlands.

Muxworthy, A. R., D. Heslop, and W. Williams (2004), Influence of magnetostatic interactions on first-order-reversal-curve (FORC) diagrams: A micromagnetic approach, *Geophys. J. Int.*, *158*, 888–897, doi:10.1016/S0012-821X(02)00880-4.

Muxworthy, A. R., J. G. King, and D. Heslop (2005), Assessing the ability of first-order reversal curve (FORC) diagrams to unravel complex magnetic signals, *J. Geophys. Res.*, *110*, B01105, doi:10.1029/2004JB003195.

Néel, L. (1949), Influence des fluctuations thermiques sur l'aimantation de grains ferromagnétiques trés fins, *C. R. Hebd. Séances Acad. Sci., Sér. B*, *228*, 664–666.

Néel, L. (1954), Remarques sur la théorie des propriétés magnétiques des substances dures, *Appl. Sci. Res. B*, *4*, 13–24.

Néel, L. (1955), Some theoretical aspects of rock magnetism, *Adv. Phys.*, *4*, 191–243.

Newell, A. J. (2005), A high-precision model of first-order reversal curve (FORC) functions for single-domain ferromagnets with uniaxial anisotropy, *Geochem. Geophys. Geosyst.*, *6*, Q05010, doi:10.1029/2004GC000877.

Novosad, V., K. Y. Guslienko, H. Shima, Y. Otani, K. Fukamichi, N. Kitakami, and Y. Shimada (2001), Nucleation and annihilation of magnetic vortices in sub-micron permalloy dots, *IEEE Trans. Magn.*, *37*(4), 2088–2090, doi:10.1109/20.951062.

Paterson, G. A., A. R. Muxworthy, A. P. Roberts, and C. MacNiocaill (2010), Assessment of the usefulness of lithic clasts from pyroclastic deposits for paleointensity determination, *J. Geophys. Res.*, *115*, B03104, doi:10.1029/2009JB006475.

Pike, C., and A. Fernandez (1999), An investigation of magnetic reversal in submicron-scale Co dots using first order reversal curve diagrams, *J. Appl. Phys.*, *85*, 6668–6676, doi:10.1063/1.370177.

Pike, C. R., A. P. Roberts, and K. L. Verosub (1999), Characterizing interactions in fine magnetic particle systems using first order reversal curves, *J. Appl. Phys.*, *85*, 6660–6667, doi:10.1063/1.370176.

Pike, C. R., A. P. Roberts, M. J. Dekkers, and K. L. Verosub (2001a), An investigation of multi-domain hysteresis mechanisms using FORC diagrams, *Phys. Earth Planet. Inter.*, *126*, 11–25, doi:10.1016/S0031-9201(01)00241-2.

Pike, C. R., A. P. Roberts, and K. L. Verosub (2001b), First-order reversal curve diagrams and thermal relaxation effects in magnetic particles, *Geophys. J. Int.*, *145*, 721–730.

Preisach, F. (1935), Über die magnetische Nachwirkung, *Z. Phys.*, *94*, 277–302, doi:10.1007/BF01349418.

Proenca, M. P., C. T. Sousa, J. Escrig, J. Ventura, M. Vazquez, and J. P. Araujo (2013), Magnetic interactions and reversal mechanisms in Co nanowire and nanotube arrays, *J. Appl. Phys.*, *113*, 093907, doi:10.1063/1.4794335.

Roberts, A. P., C. R. Pike, and K. L. Verosub (2000), FORC diagrams: A new tool for characterizing the magnetic properties of natural samples, *J. Geophys. Res.*, *105*, 28,461–28,475, doi:10.1029/2000JB900326.

Roberts, A. P., L. Chang, D. Heslop, F. Florindo, and J. C. Larrasoaña (2012), Searching for single domain magnetite in the 'pseudo-single-domain' sedimentary haystack: Implications of biogenic magnetite preservation for sediment magnetism and relative paleointensity determinations, *J. Geophys. Res.*, *117*, B08104, doi:10.1029/2012JB009412.

Roberts, A. P., D. Heslop, X. Zhao, and C. R. Pike (2014), Understanding fine magnetic particle systems through use of first-order reversal curve diagrams, *Rev. Geophys.*, *52*, 557–602, doi:10.1002/2014RG000462.

Schabes, M. E., and H. N. Bertram (1988), Magnetization processes in ferromagnetic cubes, *J. Appl. Phys.*, *64*, 1347–1357, doi:10.1063/1.341858.

Smirnov, A. V. (2006), Low-temperature magnetic properties of magnetite using first-order reversal curve analysis: Implications for the pseudo-single domain state, *Geochem. Geophys. Geosyst.*, *7*, Q11011, doi:10.1029/2006GC001397.

Smirnov, A. V. (2007), Effect of the magnetic field applied during cooling on magnetic hysteresis in the low-temperature phase of magnetite: First-order reversal curve (FORC) analysis, *Geochem. Geophys. Geosyst.*, *8*, Q08005, doi:10.1029/2007GC001650.

Stancu, A., L. Stoleriu, and M. Cerchez (2001), Micromagnetic evaluation of magnetostatic interactions distribution in structured particulate media, *J. Appl. Phys.*, *89*, 7260–7262, doi:10.1063/1.1355343.

Stancu, A., P. Andrei, and L. Stoleriu (2006), Magnetic characterization of samples using first- and second-order reversal curve diagrams, *J. Appl. Phys.*, *99*, 8D702, doi:10.1063/1.2172539.

Stoner, E. C., and E. P. Wohlfarth (1948), A mechanism of magnetic hysteresis in heterogeneous alloys, *Philos. Trans. R. Soc. London, Ser. A*, *240*, 599–642, doi:10.1098/rsta.1948.0007.

Vajda, F., and E. Della Torre (1991), Relationship between the moving and the product Preisach model, *IEEE Trans. Magn.*, *27*, 3823–3826, doi:10.1109/20.104935.

Winklhofer, M., and G. T. Zimanyi (2006), Extracting the intrinsic switching field distribution in perpendicular media: A comparative analysis, *J. Appl. Phys.*, *99*, 08E710, doi:10.1063/1.2176598.

Yamazaki, T., and M. Ikehara (2012), Origin of magnetic mineral concentration in the Southern Ocean, *Paleoceanography*, *27*, PA2206, doi:10.1029/2011PA002271.

Yu, Y., and L. Tauxe (2005), On the use of magnetic transient hysteresis in paleomagnetism for granulometry, *Geochem. Geophys. Geosyst.*, *6*, Q01H14, doi:10.1029/2004GC000839.

Zhao, X., D. Heslop, and A. P. Roberts (2015), A protocol for variable resolution first-order reversal curve measurements, *Geochem. Geophys. Geosyst.*, *16*, 1364–1377, doi:10.1002/2014GC005680.